

# The erosion of a distributed two-dimensional vortex in a background straining flow

By BERNARD LEGRAS<sup>1</sup>,  
DAVID G. DRITSHEL<sup>2</sup> AND PHILIPPE CAILLOL<sup>1,3</sup>

<sup>1</sup>Laboratoire de Météorologie Dynamique, Paris, France

<sup>2</sup>Department of Applied Mathematics, University of St Andrews, St Andrews, UK

<sup>3</sup>Now at Department of Mathematical Sciences, Loughborough University, Loughborough, UK

(Received 6 June 2000 and published in *JFM*, 2001, vol. 441, pp. 369-398)

Herein we present a simplified theory for the behaviour of a vortex embedded in a growing external straining flow. Such a flow arises naturally as a vortex moves relative to other vortices. While the strain may generally exhibit a complex time dependence, the salient features of the vortex evolution can be understood in the simpler context, studied here, of a linearly growing strain. Then, all of the typical stages of evolution can be seen, from linear deformation, to the stripping or erosion of low-lying peripheral vorticity, and finally to the breaking or rapid elongation of the vortex into a thin filament.

When, as is often the case in practice, the strain growth is slow, the vortex adjusts itself to be in approximate equilibrium with the background flow. Then, the vortex passes through, or near, a sequence of equilibrium states until, at a critical value of the strain, it suddenly breaks. In the intermediate period before breaking, the vortex continuously sheds peripheral vorticity, thereby steepening its edge gradients. This stripping is required to keep the vortex in a near equilibrium configuration.

We show that this behaviour can be captured, quantitatively, by a reduced model, the *elliptical model*, which represents the vortex by a nested set of elliptical vorticity contours, each having a (slightly) different aspect ratio and orientation. Here, we have extended the original *elliptical model* by allowing for edge vorticity levels to be shed when appropriate (to represent stripping) and by incorporating the flow induced by the vorticity being stripped away. The success of this model proves that the essential characteristics of vortex erosion are captured simply by the leading-order, elliptical shape deformations of vorticity contours.

Finally, we discuss the role of viscosity. Then, there is a competition between gradient steepening by stripping and smoothing by viscosity. If the strain grows too slowly, the vortex is dominated by viscous decay, and the edge gradients become very smooth. On the other hand, for sufficiently rapid strain growth (which can still be slow, depending on the viscosity), the vortex edge remains steep until the final breaking.

---

## 1. Introduction

Observations of the Earth's oceans and atmosphere and of other planetary atmospheres have revealed a wealth of vortices over a vast range of scales. Indeed, one may argue that these vortices largely drive the (turbulent) fluid motion. Therefore, to understand this motion, one needs to understand the behaviour of the constituent vortices, in particular their interactions with one another.

The external effects of rotation and stratification, along with the shallow geometry of geophysical flows, constrains the intermediate- and large-scale vortices to be approximately two-

dimensional, that is they exhibit strong vertical coherence. The horizontal scale above which vortices behave this way is approximately the Rossby radius of deformation,  $L_R$ , which is roughly a few hundred to a thousand kilometres in the atmosphere, and a few tens to a hundred kilometres in the ocean.  $L_R$  is proportional to the fluid depth (or the density scale height in the atmosphere) and the stratification (the buoyancy frequency), and is inversely proportional to the rate of rotation.

In the present work, we will focus on strictly two-dimensional vortices (following many previous works) as a first approximation to real geophysical vortices. Moreover, we will model the interaction between vortices (and other external forces) by a large-scale straining flow consisting of a pure (irrotational) deformation and a solid-body rotation acting on an otherwise isolated vortex. From previous works, it is known that such a flow may deform, erode or destroy the vortex according to the situation. When the vortex is taken to be simply an elliptical patch of uniform vorticity, one can find stationary (Love 1893; Moore & Saffman 1971) and periodic (Kida 1981) solutions analytically for steady rates of deformation and rotation. Beyond a critical rate of deformation (hereafter “strain”), the vortex extends indefinitely as a thinning vorticity strip. The stability of these solutions (to non-elliptical deformations) was considered by Dritschel (1990), who found that instability occurs in relatively inaccessible parts of the parameter space. It is noteworthy that “breaking”, the indefinite extension of the vortex, occurs without the prior generation of filaments — the vortex tends to keep its elliptical form. This is in contrast to vortex merger, for example, in which filaments are generated around the compound vortex as a result of the strongly varying strain field felt by each vortex. This is also in contrast to the behaviour of *distributed* vortices, which tend to shed their external layers of low-lying vorticity as thin filaments that get pulled away by the background flow (Legras & Dritschel 1993*a*; Dritschel & Waugh 1992). A consequence of this is the generation of steep vorticity gradients at the vortex periphery which are only weakly smoothed by dissipation when the Reynolds number is large (Legras & Dritschel 1993*b*; Mariotti, Legras & Dritschel 1994; Yao, Dritschel & Zabusky 1995). These gradients are actually directly observed in geophysical flows as gradients of chemical species which can be measured with much higher resolution than vorticity (or potential vorticity) itself. It is remarkable that aircraft sections of the polar stratospheric vortex exhibit large jumps in ozone and other gas concentrations over distances of just two kilometres or so — the resolution of the measurements — when crossing through the edge of the vortex (Tuck 1989).

The main goal of this paper is to study the erosion of a distributed vortex and to provide a theoretical description for it based on the elliptical model developed in Legras & Dritschel (1991). In most studies so far (Kida 1981; Legras & Dritschel 1993*a*), the external strain has been applied as a finite-amplitude perturbation to an initially circular vortex or was left constant with time (Dritschel 1990). This situation is unrealistic since the vortex is likely to experience strain growth over a finite time. In this study, we will consider the case of a linear growth of the strain from zero to the value at which the vortex breaks. In practice, the strain variations can be much more complex but the main steps of the evolution can be understood by a linear growth. This study will focus principally on the inviscid mechanisms which are responsible for vortex erosion and breaking. The viscous decay of a vortex submitted to a fixed strain has been studied by Jimenez, Moffatt & Vasco (1996). The case of slowly growing strain was considered by Mariotti *et al.* (1994), who showed that the main characteristics of inviscid erosion are preserved. Below, we show that there is a continuous transition between viscous decay and inviscid erosion that depends on the strain growth for a given viscosity.

In §§ 2 and 3 we formulate the basic problem, illustrate simulations of both weakly viscous and inviscid vortex erosion, and indicate various properties of this erosion that are relevant to the theory to follow. Section 4 reviews the elliptical model and presents several extensions to it that are necessary to describe erosion quantitatively. This approximate model greatly reduces the complexity of the original system and is central to the proposed theory. Section 5 compares

the results with inviscid numerical simulations carried out with “contour surgery”. Here, we also describe one curious simulation for an extremely slow strain growth that exhibits an unexpected degree of unsteadiness. Section 6 discusses the role of viscosity. In particular, we connect the regimes of pure viscous decay (when the strain is steady) to inviscid erosion (when the strain growth is rapid enough). Finally, § 7 offers our conclusions.

## 2. Vortex stripping

A general linear external straining flow can be expressed simply using complex notation as

$$u_{ext} + iv_{ext} = -i\gamma\bar{z}\exp(2i\phi_s) + i\Omega z, \quad (2.1)$$

where  $z = x + iy$  and  $\bar{(\ )}$  stands for complex conjugation. By convention,  $\gamma$  is positive and the orientation of the strain is defined by  $\phi_s$ . We focus attention to the two particular cases of *pure strain*, i.e.  $\Omega = 0$ , and of *adverse shear*, i.e.  $\Omega = -\gamma$ .

The initial condition is a circular vortex. Two radial vorticity profiles are considered, the Gaussian

$$\omega_v(r) = \omega_0 \exp\left(-r^2/r_0^2\right),$$

which is a solution for pure viscous decay, and the parabolic

$$\omega_v(r) = \omega_0 \left(1 - (r^2/r_0^2)\right),$$

for  $r < r_0$  which is generic near the centre of a non-uniform vortex. In both cases without loss of generality we take  $\omega_0 > 0$ , i.e. positive vorticity.

The strain grows linearly in time according to  $\gamma(t) = \omega_0 t/\tau$ . The growth is slow when the variation of  $\gamma$  over a rotation period  $T$  of the vortex ( $T \approx 2\pi/\omega_0$ ) is small compared to the critical strain required to break the vortex. As the latter is typically of the order of  $\omega_0/10$  both for pure strain and adverse shear, the condition of slow growth is that  $\omega_0 T/\tau \ll \omega_0/10$ , that is  $1/\tau \ll \omega_0/50$ . In what follows we often use the dimensionless strain  $\gamma^* = \gamma/\omega_0$ .

Numerical simulations have been performed using both the pseudo-spectral (PS) and the contour surgery (CS) methods. The two methods have been compared in Legras & Dritschel (1993a) for a vortex street subjected to uniform, constant shear. Excellent agreement was shown when only eight contours were used in the CS method to discretize the vorticity distribution, and when sufficiently high grid resolution was used in the PS method. Here we use the same or better resolution in each method. The PS method uses a doubly periodic domain, of dimension  $2\pi \times 2\pi$ , and with sponge layers on the edges to absorb outgoing vorticity to approximate an infinite domain (for details, see the appendix of (Mariotti *et al.* 1994)). A small viscosity is included both to stabilize the numerical method and to permit us to explore the role of viscosity in vortex erosion. The CS method simulates directly the vortex evolution on the infinite plane using the Green function of Laplace’s operator and a Lagrangian representation of the equations of motion. By discretizing the vorticity into uniform regions (which may be nested), the flow evolution reduces entirely to the motion of the contours across which the vorticity jumps. This Lagrangian representation remains valid only for inviscid dynamics. In practice, contours become highly convoluted and it is necessary to limit their complexity by “surgery”, or the removal of vorticity filaments below a prescribed scale (Dritschel 1989). Notice that the two methods are used here for their complementary possibilities: CS as a reference for the inviscid theory to follow; PS to validate this approach under the effect of small viscosity.

In the first simulation using the PS method (experiment 1), the resolution of the collocation grid is  $512 \times 512$  with an isotropic truncation at wavenumber  $k_{\max} = 256$ . The vortex is initially Gaussian with  $r_0 = 0.5$  and  $\omega_0 = 2\pi$ . It is subjected to an adverse shear,  $u = 2\gamma(t)y$  (i.e.  $\phi_s = \pi/2$  and  $\Omega = -\gamma$ ) growing at the rate  $1/\tau = 0.0014$ . A small viscosity  $\nu = 4.6 \times 10^{-5}$  is included,

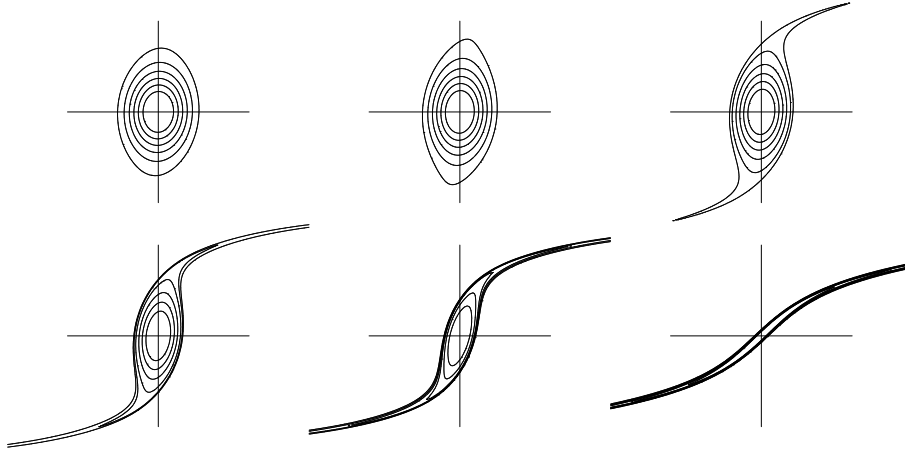


FIGURE 1. Vorticity charts at times  $t = 26, 31, 36, 41, 46, 51$  from left to right and from top to bottom for experiment 1, conducted using the PS method with a small viscosity. The vortex is initially Gaussian and is subjected to a linearly growing adverse shear. The contour interval is 0.8.

corresponding to a Reynolds number  $Re = \omega_0 r_0^2 / \nu = 34,000$ . There are initially 82 collocation points across the vortex, a resolution far greater than that commonly used in simulations of turbulence initialized with a large number of vortices, yet far less than that required to resolve a true atmospheric or oceanic vortex.

Figure 1 shows the evolution of the vortex at selected times. During the first stage of the erosion, the vortex elongates while it remains closely aligned with the  $y$ -axis. At time  $t = 31$ , the most exterior contour exhibits relatively high curvature at its tips ( $y$  extremities) in response to the approaching critical points of the streamfunction (stagnation points of the velocity field). As these points cross the periphery of the vortex, a filament forms and is expelled into the background flow (eventually to be absorbed by the sponge layer). As time proceeds and the shear grows, higher level vorticity contours are entrained within the filament, leaving an increasingly sharp edge at the vortex periphery (limited only by viscosity). Finally, at a critical value of the shear, the vortex core breaks by suddenly rotating into the extensional direction of the straining flow where it is rapidly elongated.

Figure 2 shows the evolution of the vorticity cross-section taken along the  $x$ -axis. The initially Gaussian profile slightly flattens due to the effect of viscosity but, first and foremost, it exhibits a steep gradient at the vortex edge which moves inwards as the strain grows. The vorticity contours are stretched by the production of the filaments and, by continuity, they pile up on the vortex edge as seen in figure 1. The vortex edge width however cannot collapse indefinitely due to viscosity (see § 6).

In the second simulation, conducted using the CS method (experiment 2), the vortex is initially parabolic with  $r_0 = 1$  and  $\omega_0 = 2\pi$ . A pure strain, with  $\phi_s = \pi/2$ , is applied, growing at the rate  $1/\tau = 2.5 \times 10^{-4}$ . The vorticity profile is represented by  $n = 20$  discrete steps, located initially at the radii  $r_k = (k/n)^{1/2}$ , and the vorticity jumps by  $\Delta\omega = \omega_0/n$  across each step except for the outermost one, where it jumps by  $\Delta\omega/2$ . This discretization ensures that the velocity of the discrete and the continuous profiles match at the contour locations. This number of contours is more than adequate to accurately capture the dynamics of the vortex, as shown in Legras & Dritschel (1993a) and Dritschel (1998). Along each contour, points are distributed, and periodically redistributed, as described in Dritschel (1989), using the large-scale length  $L = r_0 = 1$ , dimensionless maximum node separation parameter  $\mu = 0.08$ , and surgical scale  $\delta = \mu^2 L/4 = 0.0016$ , corresponding to 1250 surgical lengths spanning the diameter of the initial vortex.

Figure 3 shows the evolution of the vortex. The evolution is strikingly similar to that for ad-

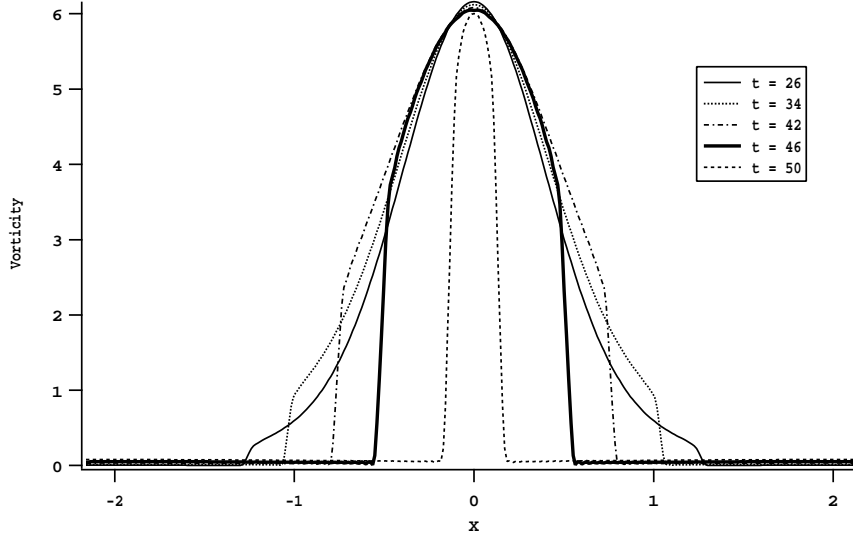


FIGURE 2. Vorticity section along the  $x$ -axis for experiment 1 at several times as indicated in the legend.

verse shear already seen in figure 1, except that the duration of the erosive phase relative to the breaking time is now shorter, owing to the steeper initial vorticity profile, and that the filaments are expelled along the diagonal. This diagonal is the extensional axis of the strain, and filaments are stretched exponentially along it. In the case of adverse shear, by contrast, only linear stretching is possible, and this does not occur along the extensional axis of the strain (again the diagonal). The filaments are instead deflected towards the  $x$ -axis, i.e. parallel to the shear flow. But what is most important here is that the vortex cores in each case consist of approximately elliptical contours in near-alignment with the  $y$ -axis.

The near-alignment of the vortex with the  $y$ -axis suggests that the vortex is tracking through (or near) equilibrium states associated with the instantaneous straining flow. Such states, discussed below, are perfectly aligned with the  $y$  axis. The tendency for vortices to remain close to equilibrium states when the external flow is changing slowly was also noted in Mariotti *et al.* (1994) and exploited in Dritschel (1995), who showed that strong vortex interactions (like merger) may be triggered by the transition from a stable to a marginally unstable equilibrium state. This idea is re-examined below in the context of vortex erosion to understand the final breaking.

Figure 4 shows contours extracted from figure 3 at times  $t = 57$  and  $63$ . For each time two contours are shown, one being on the verge on erosion and one inside the vortex, and the fitting ellipses are superimposed. The agreement is excellent for the two interior contours and remains good even on the edge and close to the final breaking ( $t = 63$ ).

After breaking, the vortex undergoes fast extension into a thin filament aligned with the strain axis (the  $x$ -axis in experiment 1 and the main diagonal in experiment 2) which is halted by dissipation in experiment 1 when it reaches a transverse scale of order  $(\nu/\gamma)^{1/2}$ . This is only true under the assumption of a background uniform strain. Within a more realistic large-scale flow, the remains of the vortex would soon separate into multiple pieces.

The fitting ellipses are calculated using the moments of the vorticity contours. For a given contour  $C$  enclosing the area  $S$  we define

$$\alpha_n = \int \int_S z^{n-1} dx dy = \frac{i}{2n} \oint_C z^n d\bar{z}, \quad (2.2)$$

with  $z = x + iy$ . The area of the contour is given by  $\alpha_1$  and, when the contour is an ellipse,  $\alpha_3$

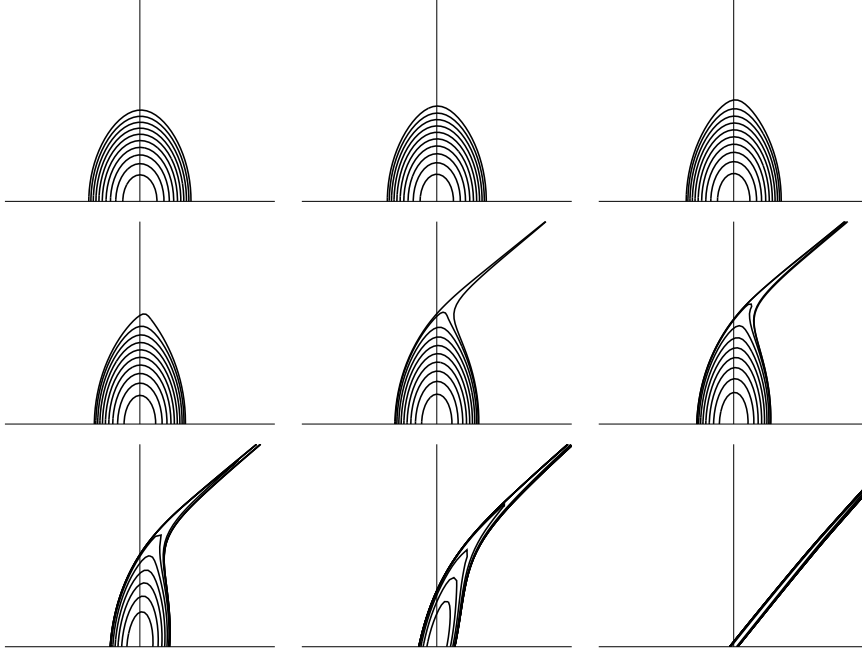


FIGURE 3. Vorticity charts at times  $t = 42, 45, 48, 51, 54, 57, 60, 63, 66$  from left to right and top to bottom for experiment 2, conducted using the CS method. The vortex is initially parabolic and is subjected to a linearly growing pure shear. All 20 contours are plotted but several contours at the vortex edge have become indistinguishable as a result of stripping.

provides the eccentricity  $\sigma$  and the orientation  $\phi$  of the contour by

$$\frac{\sigma}{1 - \sigma^2} = \frac{\pi|\alpha_3|}{\alpha_1^2} \quad (2.3)$$

$$\phi = \frac{1}{2} \arg \alpha_3. \quad (2.4)$$

The fifth moment can be used to test the deviation from an elliptical shape. More precisely the residual fifth moment

$$\alpha'_5 = \frac{\alpha_5 \alpha_1}{\alpha_3^2} - 2 \quad (2.5)$$

vanishes for an ellipse. Figure 5 shows the temporal evolution of  $|\alpha'_5|$  for several contours taken from experiment 2, including the most interior and the most exterior ones. It is clear that all contours depart only slightly from an elliptical shape until they are eroded — this property is used in the elliptical model (see § 4). The fast growth associated with erosion is followed by saturation and a fall, due to the appearance of elongated filaments. Notice that the departure from ellipticity is larger for exterior contours. This is because the velocity induced by an ellipse of uniform vorticity is linear in  $x$  and  $y$  inside the ellipse and thus preserves the elliptical shape of any embedded ellipse, whereas the velocity field is nonlinear outside the ellipse (Legras & Dritschel 1991). Therefore, the effect of interior vorticity is to slightly distort the exterior contours from an elliptical shape.

Figure 6 shows the vorticity field and selected streamlines in the vicinity of the departing filament for experiment 1 at  $t = 42$ . The four selected streamlines meet at the critical point where the velocity vanishes and are therefore the separatrices of the flow. The two interior separatrices are closed and connected to the other critical point on the other side of the vortex, while the two

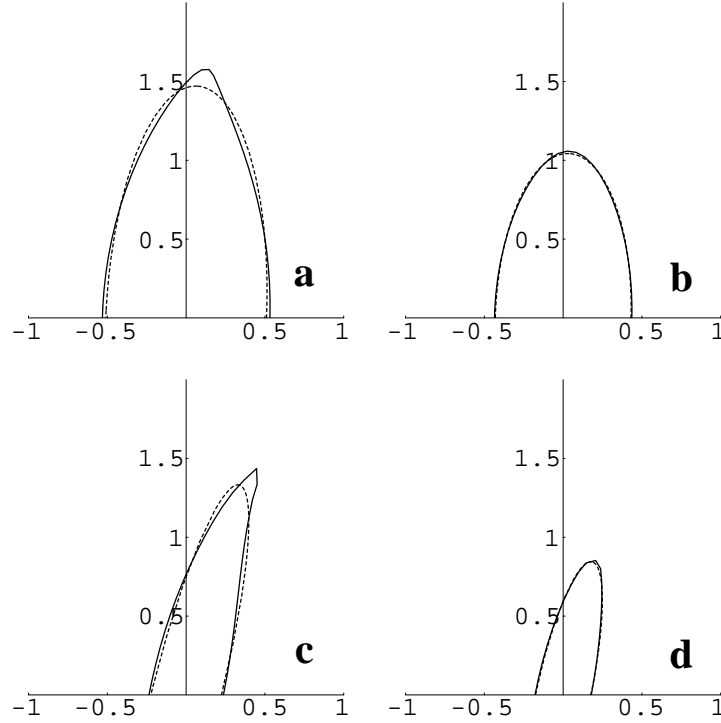


FIGURE 4. Vorticity contours (solid) and fitted ellipses (dotted) for experiment 2. Upper row:  $t = 57$ , and (a)  $\omega = 0.25\omega_0$  (contour 6), (b)  $\omega = 0.55\omega_0$  (contour 12). Lower row:  $t = 63$ , and (c)  $\omega = 0.7\omega_0$  (contour 15), (d)  $\omega = 0.85\omega_0$  (contour 18).

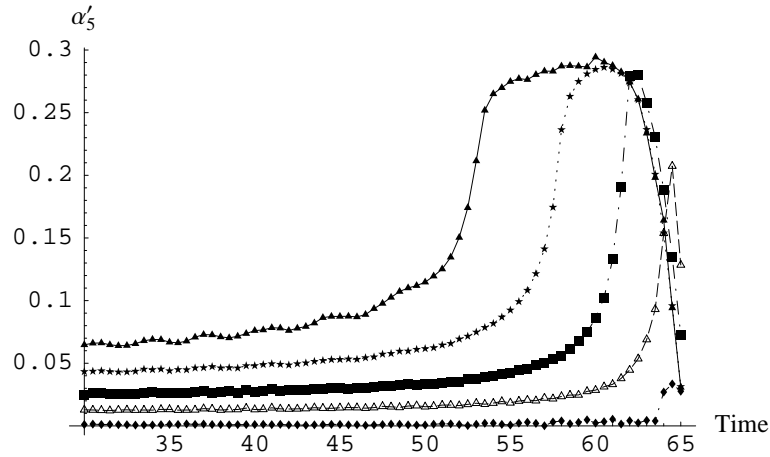


FIGURE 5. Residual fifth-order moment  $|\alpha'_5|$  as a function of time ( $t > 30$ ) for various vorticity contours in experiment 2:  $\blacklozenge$ ,  $\omega = 0$  (contour 1);  $\blacktriangle$ ,  $\omega = 0.2\omega_0$  (contour 5);  $\blacksquare$ ,  $\omega = 0.45\omega_0$  (contour 10);  $\blackstar$ ,  $\omega = 0.7\omega_0$  (contour 15); and  $\blacktriangleup$ ,  $\omega = 0.95\omega_0$  (contour 20).

exterior separatrices are open to infinity (or to the edge of the simulated domain). If this pattern were frozen in time, and if the viscosity were negligible, fluid particles inside the two interior separatrices would remain trapped there while those outside would leave the vicinity of the vortex on a trajectory roughly parallel to the outgoing exterior separatrix on the upper right side or its

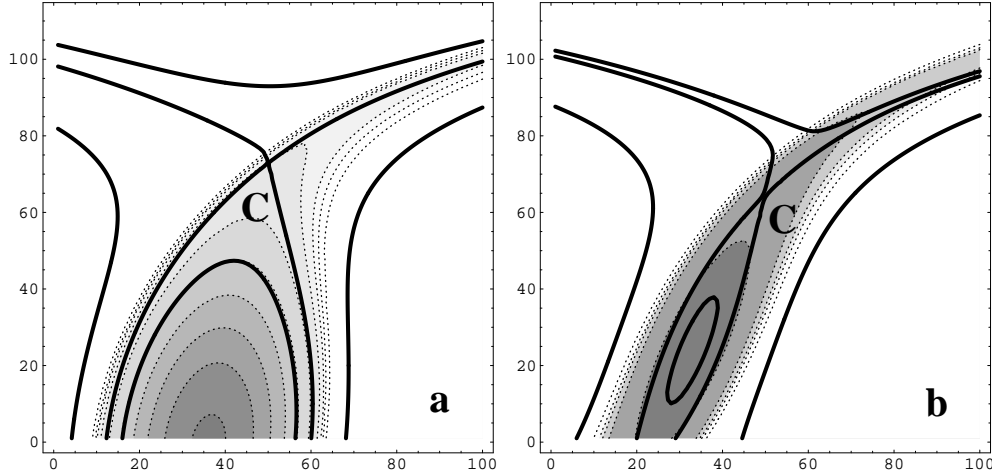


FIGURE 6. (a) Enlargement of the vorticity chart at  $t = 42$  for experiment 1. Thick solid line: the separatrices, crossing at the critical point  $C$ , and other selected streamlines. Dotted line: vorticity contours with contour interval  $0.1\omega_0$ . Axis labels are in units of the collocation grid. (b) Same but at  $t = 48$  and with a contour interval  $0.2\omega_0$ . The enlarged window has the same size in (a) and (b) but has a different centre.

image across the vortex on the lower left side. Fluid particles initially above and to the left of the critical point but to the right of the incoming exterior separatrix would move downwards towards the vortex initially before moving out along the outgoing separatrix. If the vorticity shown in this figure were a passive tracer, then after a short period of time, only the tracer within the two interior separatrices would be visible. It is useful to regard this interior region as the vortex core. Under the action of viscosity, but still keeping the velocity field frozen, a boundary layer of width  $O(v^{1/2})$  would develop on the edge and the vorticity, here considered as a passive tracer, would slowly diffuse across the edge and be expelled away. This problem is considered below in § 6.

Now consider the real situation where the pattern varies, that is when the critical points slowly penetrate the vortex. This inward motion occurs first because the strain is growing in time and second because the vortex core loses circulation. Consequently, the line of highest vorticity gradient lies slightly outside the interior separatrix on the incoming (left) side of the critical point. This highest gradient line extends continuously to the expelled filament on the right-hand side of the figure and there closely corresponds to the outgoing exterior separatrix. Notice that the incoming exterior separatrix suddenly changes its orientation as it crosses the highest gradient line as a consequence of the vorticity jump. On the right-hand side of the figure, the interior separatrix and the highest gradient line (marked by the three closely packed contours) do not coincide. Instead, this line diverges from the interior separatrix and converges to the exterior separatrix. The fluid left between the separatrices and the highest gradient line is being expelled via the filament. The nearly stagnant fluid around the critical point is put into motion and expelled by the inward motion of the critical point. In this way, the vortex continues to erode.

It is apparent from figure 6(a) that the streamlines nearly coincide with the vorticity lines inside the vortex and on its edge, with the only significant departures occurring around the corner (the vicinity of the critical point  $C$ ) and within the expelled filament. This indicates that the vortex core (the region within the interior separatrix) may be very close to an equilibrium state over most of its evolution. It is only during the very last stage of breaking or sudden elongation that this quasi-stationary assumption fails. Figure 6(b), at  $t = 48$ , shows that the separatrices in this last stage are no longer located near the vortex edge but retreat rapidly towards the vortex centre. Moreover, the interior streamlines no longer coincide with the vorticity contours there. The flow

is now highly unsteady and rapidly leads to vortex breaking (see figure 1). Similar results for collapsing vortices were found in Dritschel (1995).

### 3. Breaking of a uniform elliptical patch

Some features of the evolution of a distributed vortex described above are shown next to be found also in the evolution of a perfectly elliptical vortex patch. There are important exceptions, but the elliptical vortex serves to highlight these as well. Consider then an ellipse of uniform vorticity  $\omega$ , eccentricity  $\sigma$ , and angle  $\phi$  (with respect to the  $x$ -axis) embedded in the external flow given by (2.1). Using the complex variable  $m \equiv 2(1/\sigma - \sigma)^{-1} \exp(-2i(\phi - \phi_s))$ , the exact equation of motion is

$$\frac{d}{dt}m = 2i\gamma \frac{1 + \sigma^2}{1 - \sigma^2} - 2im \left( \Omega + \frac{1}{4}\omega(1 - \sigma^2) \right), \quad (3.1)$$

which ensures that the elliptical shape is preserved. Equation (3.1) is easily derived from the evolution equations for  $\phi$  and  $\sigma$  (Love 1893; Kida 1981). It has been shown by Legras & Dritschel (1991) that the phase and the argument of  $m$  are conjugate canonical variables and that the argument is proportional to the total impulse. The linear and nonlinear stability of this flow has been studied by Dritschel (1990), who showed that it may be unstable to non-elliptical deformations depending on the precise values of  $\gamma$ ,  $\Omega$  and the initial state (the value of  $m(0)$ ). However, the part of parameter space in which instability occurs is relatively inaccessible in practice, and for instance it does not include pure strain or adverse shear. The filamentation seen for a distributed vortex is not evidence of this instability, but simply the kinematic consequence of the fact that the critical points do not remain clear of the vortex boundary but attempt to penetrate inside. The filaments are a direct parametric response to the external strain.

The near alignment of the vortex with the  $y$ -axis during most of the erosion, noted in the previous section, can be understood from the behaviour of the elliptical patch. For short time  $t \ll \tau$ , the solution to (3.1) for adverse growing shear and with  $m(0) = 0$  is

$$m(t) = \frac{4t}{\tau} + \frac{8i}{\omega\tau} (1 - e^{-i\omega t/2}) + O\left(\frac{t^3}{\tau^3}\right) \quad (3.2)$$

— a cycloidal motion tangent to the real axis in  $m$ -space. When  $\tau\omega$  is large, the oscillation occurs around a mid-trajectory  $\langle m \rangle(t) = 4t/\tau + 8i/(\omega\tau)$  which departs slightly from the instantaneous equilibrium position on the real axis. The numerical solution to (3.1) is shown in figure 7(a) for  $\omega = 0.6 \times 2\pi$  and  $1/\tau = 0.0014$  as in experiment 1. The cycloidal motion of the small-time solution continues at larger times but the mid-trajectory departs more strongly from the real axis than does  $\langle m \rangle$ . The oscillations do not grow until immediately before the final breaking, that is the fast elongation of the vortex into a thin filament. This breaking occurs at a value of the strain which is very close to the limiting strain beyond which stationary, equilibrium solutions do not exist. Breaking is therefore associated with the loss of equilibrium solutions at higher values of the strain rate.

The angular deviation of the ellipse from its equilibrium orientation, shown in figure 7(b), is  $\pi/4$  for  $t = 0$  but remains small, of  $O(\omega^{-1}t^{-1})$  and negative during most of the evolution prior to the final breaking as long as (3.2) is valid. The negative angle ensures that the vortex continues to elongate as the strain grows. The same behaviour is seen in figure 7 for experiment 1, where  $m$  is calculated as  $m = 2\pi\alpha_3\alpha_1^{-2}$  for an intermediate contour of the distributed vortex, though the oscillations are much reduced in amplitude and less regular. Notably, when the strain is fixed in time, the angle strongly oscillates about zero and the vortex does not elongate. The evolution of a vortex subjected to a slowly growing strain, on the other hand, remains trapped within a small neighbourhood of the evolving instantaneous equilibrium until final breaking.

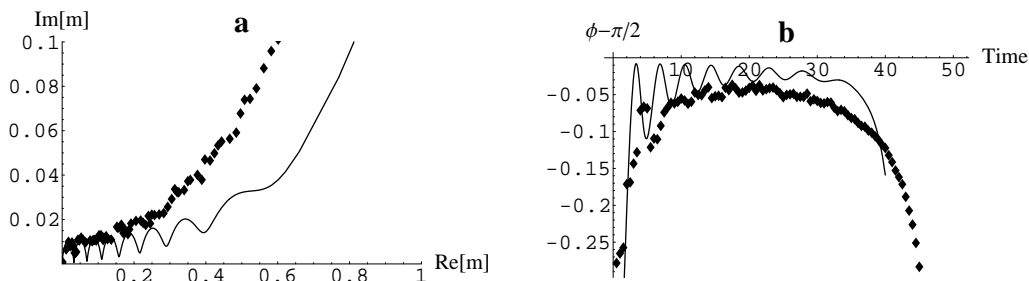


FIGURE 7. (a) Solid line: evolution of the solution to (3.1) in the  $m$ -plane for  $\omega = 0.6 \times 2\pi$  and  $1/\tau = 0.000014$ .  $\blacklozenge$ :  $m(t)$  calculated for the contour  $\omega = 0.6 \times 2\pi$  in experiment 1. (b) Same as (a) except the evolution of  $\phi - \pi/2$  is shown.

## 4. The elliptical model

### 4.1. The basic model

To study the effects of varying vorticity, we need to go beyond the elliptical vortex patch. For instance, we may wish to represent the vortex, approximately, by a nested stack of elliptical disks of uniform vorticity, to keep as close as possible to the idealized but exact solution available for the single elliptical patch. Such a model, called the ‘‘Elliptical Model’’ (EM) was derived earlier in Legras & Dritschel (1991). It is approximate because the elliptical shapes of the vorticity contours are not exactly preserved if contours are embedded within each other, or are separated from one another. Nevertheless, the errors are small so long as vortices are well separated (if there are multiple vortices) or if the foci of embedded elliptical contours in a vortex vary slowly with mean contour radius. This approximation is supported well by the results of § 2 and by simulations of turbulence (Jimenez *et al.* 1996).

In the elliptical model, each elliptical disk is characterized by its area  $\pi r^2$ , which defines the mean radius  $r$ , and its vorticity  $\omega$ , both conserved under inviscid evolution. We define  $\lambda$  to be the aspect ratio of the ellipse,  $\sigma$  to be its eccentricity and  $\phi$  to be its orientation. A distributed vortex is built by superposing, or embedding, disks. In the continuous limit, we integrate, over the variable  $r$ , each elementary disk of vorticity  $(-d\omega/dr)\delta r$ . We assume that the vortex has a finite extent and denote the radius of the outermost disk by  $R$ .

For an isolated vortex in a straining flow, only two parameters are useful for describing the dynamics of the system, for example  $\sigma(r, t)$  and  $\phi(r, t)$ . They obey two differential equations containing three contributions:

- (a) the external straining flow,
- (b) the disks external to and including a particular disk  $\omega(r)$ , and
- (c) the disks internal to a particular disk  $\omega(r)$ .

It is the last contribution which is approximate; the EM only considers that part of the flow field generated by the internal disks which preserves the elliptical shape of the particular disk. Summing these three contributions and passing to the continuous limit, the equations governing the evolution of a strained vortex are

$$\begin{aligned}
\frac{\partial}{\partial t} m(r) = & -2i\Omega m(r) + 2i\gamma \frac{1 + \sigma^2(r)}{1 - \sigma^2(r)} + im(r)\omega(r) \\
& - i \frac{1}{2r^4} \int_0^r s^4 m(s) \omega'(s) ds + i \frac{1 - \sigma^2(r)}{r^2} \int_0^r s^2 \omega'(s) ds \\
& - i \frac{1 + \sigma^2(r)}{2(1 - \sigma^2(r))} \int_r^R \omega'(s) m(s) (1 - \sigma^2(s)) ds \\
& + i \frac{(1 - \sigma^2(r))^2}{8r^4} \int_0^r s^4 \overline{m} \omega'(s) ds \\
& + i \frac{1 + \sigma^2(R)}{2(1 - \sigma^2(R))} \omega(R) m(R) (1 - \sigma^2(R)),
\end{aligned} \tag{4.1}$$

where  $\omega' = d\omega/dr$  and the dependence on  $t$  (though implicit) has been suppressed for  $\sigma$  and  $m$ , as defined in (3.1).

In spite of its apparent complexity, (4.1) is a considerable simplification over the original Euler equations since it reduces a two-dimensional problem (depending on two space coordinates) by one dimension. It is used here to describe the dynamics of the vortex interior and is solved by a numerical discretization of the vorticity profile into  $N$  disks. In a companion paper (Caillol and Legras, 2000, preprint) the solution to (4.1) is obtained by a low-order truncation of a Tchebychev expansion of  $\sigma(r)$  and  $\phi(r)$ . Since contours are ellipses, an obvious limitation of the EM is its inability to generate the corners observed near the critical points. It will be apparent below that these corners have a crucial effect on the erosion and the breaking of the vortex. Hence, we need to supplement the EM with a model of the corner and to calculate the erosion within this framework, using reasonable assumptions and approximations.

#### 4.2. Modelling the corner

We first assume that the location of the critical point is at a distance  $X_C$  from the center along the principal axis of the exterior contour. The assumed geometry of the corner, illustrated in figure 8, is based on the observations made in § 2 (see in particular figure 6(a)). The corner is bounded by the two tangents from the critical point  $C$  to the exterior ellipse and by the arc  $PP'$ . We further approximate the arc  $PP'$  by a circular arc. Then, the corner is fully characterized by its angle  $\theta$  and the length  $\chi$  of its two sides, given in Appendix A, § A.1. The corner is assumed to contain uniform vorticity equal to the value  $\omega(R)$  associated with the exterior ellipse.

Now we need to satisfy the condition of vanishing velocity at the critical point and take into account the contribution of the two opposite corners to the EM. The geometric assumptions which define the corners lead to analytical formulae after a few simple but lengthy algebraic manipulations. We leave the detailed derivation to the appendices and give here the essential results.

If we neglect the mis-alignment of the ellipses and suppose that they are all oriented at the same angle  $\phi$ , the contribution of the elliptical vortex to the velocity normal to the principal axis  $V$  at a distance  $X$  from the vortex centre is (Legras & Dritschel 1991)

$$V_v(X) = \frac{\omega(R)R^2}{X(1 + \cos v_r)} - \int_0^R \frac{\omega'(r)r^2}{X(1 + \cos v_r)} dr, \tag{4.2}$$

where  $v_r$  is given by

$$\sin v_r = 2 \frac{r}{X} \left( \frac{\sigma(r)}{1 - \sigma^2(r)} \right)^{1/2}. \tag{4.3}$$

Notice that the variation  $d\phi/dr$  of ellipse orientation and  $d\sigma/dr$  are bounded by the no-crossing

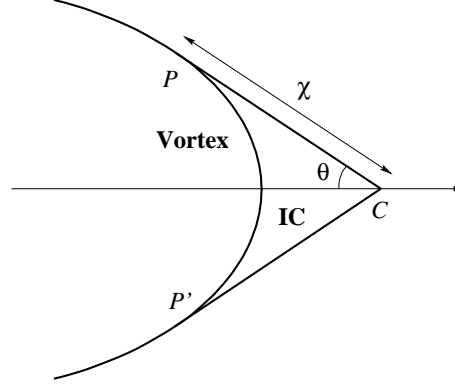


FIGURE 8. Sketch of the corner near the critical point as idealized for use in the EM+C.

condition for the ellipses

$$(\sigma^2 + 1)^2 \left( \frac{d\sigma}{dr} \right)^2 + 16\sigma^2 \left( \frac{d\phi}{dr} \right)^2 < \frac{4}{r^2} (1 - \sigma^2)^2.$$

In practice  $|\frac{d\phi}{dr}|$  is small and its contribution to  $V_v$ , which is  $O((\frac{d\phi}{dr})^2)$ , is neglected here.

By adding the contribution (4.2) to that of the strain and that of the corners  $V_c + V_{\text{opp}}$  given in Appendix A, § A.2, the condition of zero normal velocity at the critical point gives the following equation for  $X_C$ :

$$V(X_C) \equiv V_v(X_C) + (\Omega - \gamma \cos 2(\phi - \phi_s))X_C + V_c(X_C) + V_{\text{opp}}(X_C) = 0. \quad (4.4)$$

Finally, we take into account the contribution of the corners to the elliptical model (cf. Appendix A, § A.3), completing the corner-augmented model, hereafter denoted as “EM+C”.

#### 4.3. Modelling the erosion

The last step is to provide a condition for the erosion. Before the onset of erosion, the separatrix area is larger than that of the most exterior ellipse. After the onset of erosion, it is apparent from figure 6(a) that the line of highest gradient follows the separatrix except in the close vicinity of the corner. The erosion condition is then obtained by matching the area of the most exterior ellipse with that of the separatrix. This approximation is valid as long as the evolution is slow enough to be considered quasi-stationary, that is up until the final breaking.

In order to calculate the streamfunction  $\psi$ , it is convenient to use coordinates  $(X, Y)$  referred to the axis of the vortex. Then the contribution of the elliptical vortex core to  $\psi(X, Y)$  is

$$\begin{aligned} \psi_v(X, Y) = & - \int_0^R \frac{\omega'(r)r^2}{2} \Re \left[ \frac{1}{2} \tan^2\left(\frac{1}{2}u\right) - \ln \tan^2\left(\frac{1}{2}u\right) \right] dr \\ & + \frac{\omega(R)R^2}{2} \Re \left[ \frac{1}{2} \tan^2\left(\frac{1}{2}u_R\right) - \ln \tan^2\left(\frac{1}{2}u_R\right) \right], \end{aligned} \quad (4.5)$$

where

$$\sin u = 2 \frac{r}{X + iY} \left( \frac{\sigma(r)}{1 - \sigma^2(r)} \right)^{1/2}.$$

By adding to (4.5) the contribution of the strain and that of the corners  $\psi_C(X, Y)$  given in Appendix A, § A.4, we have

$$\begin{aligned} \psi(X, Y) = & \frac{1}{2}\Omega(X^2 + Y^2) + \frac{1}{2}\gamma(Y^2 - X^2) \cos 2(\phi - \phi_s) \\ & + \gamma XY \sin 2(\phi - \phi_s) + \psi_v(X, Y) + \psi_C(X, Y). \end{aligned} \quad (4.6)$$

Therefore, the streamfunction at the critical point is

$$\begin{aligned} \psi(X_C, 0) &= \frac{1}{2}(\Omega - \gamma \cos 2\phi)X_C^2 + \psi_v(X_C, 0) \\ &+ \omega(R) \left\{ \psi_c(\theta, \chi) + \frac{A(\theta, \chi)}{2\pi} \ln[2X_C + \hat{X}(\theta, \chi)] \right\}. \end{aligned} \quad (4.7)$$

After calculating the value of the streamfunction at the critical point one may find other points on the separatrix by solving  $\psi(X, Y) = \psi(X_C, 0)$ . The separatrix is then parametrized as a combined set of polynomial curves and its area  $\mathcal{A}_S$  is obtained as indicated in Appendix B.

The erosion condition is given by

$$\mathcal{A}_S \geq \pi R^2, \quad (4.8)$$

where the inequality is strict before the onset of erosion for a bounded vortex and the equality applies during the erosion as long as the strain is growing monotonically. It then determines the equivalent radius  $R(t)$  of the vortex edge.

#### 4.4. The parabolic vortex

Because of the weighting factor  $\omega'(r)r^2$  within the integrals of (4.2) and (4.5), most of the contribution to  $\psi_v$  and  $V_v$  arises from the vicinity of the edge. Moreover, if we neglect the variations of  $\sigma$  inside the vortex, assuming a constant value  $\sigma = \langle \sigma \rangle = \sigma(R)$ , and if we limit our scope to a parabolic vorticity profile with  $\omega_0 = 1$  and  $r_0 = 1$ , the integrals in (4.2) and (4.5) can be calculated analytically. We have

$$V_v = \frac{(1 - \langle \sigma \rangle^2)X_C}{2\langle \sigma \rangle} \left( \sin^2(\frac{1}{2}v_R) + \frac{R^2}{6}(2\sin^2(\frac{1}{2}v_R) - 3)\tan^2 \frac{1}{2}v_R \right), \quad (4.9)$$

$$\begin{aligned} \psi_v &= \Re \left[ \left( \frac{1}{2} \tan^2(\frac{1}{2}u_R) - \ln \tan(\frac{1}{2}u_R) \right) R^2 + \left( \frac{1}{4} \ln \tan(\frac{1}{2}u_R) \right. \right. \\ &\quad \left. \left. + \frac{1}{192}(1 + 8 \cos u_R + 3 \cos 2u_R) \sec^4(\frac{1}{2}u_R) R^4 \right] \right]. \end{aligned} \quad (4.10)$$

#### 4.5. The complete elliptical model

The complete elliptical model used in what follows consists of the set of equations (4.1), (4.4), (A 8) and (4.8). The vortex is discretized into 200 equally spaced vorticity levels, and for each contour the radius  $r$  is chosen to match the circulation of the corresponding continuous profile at  $r$ .

The initial condition is a circular vortex. The strain grows linearly in time from zero just as in the two experiments presented in § 2. During the first stage of the evolution, the vortex wobbles slightly and gradually elongates while its mean radius  $R$  remains constant. This stage is modelled using the original EM (4.1) without any corner correction. The location of the critical point and the separatrices are calculated and are found to lie beyond the vortex — the inequality (4.8) is strictly satisfied. This stage ends when the separatrix hits the vortex and the equality in (4.8) is first satisfied.

From this time, we use the EM+C to determine the evolution of the ellipses, as well as the location of the critical point and the separatrix. When the condition (4.8) is violated, the radius  $R$  is reduced by removing the exterior disk of the vortex. The numerical procedure for one time step consists of the following:

(a) Integrate in time (4.1) with the corner contribution (A 8) after solving (4.4) for the location  $X_C$  of the critical point. These operations are performed during each step of a fourth-order Runge–Kutta integrator using a time step  $\Delta t = 0.02$ .

(b) Calculate the location of the separatrix by solving  $\psi(0, Y_S) = \psi(X_C, 0)$  and  $\psi(X_i, Y_i) = \psi(X_C, 0)$  using (4.7) and (A 9), and compute its area using (B 1).

(c) If (4.8) is not satisfied, remove exterior contours until (4.8) is and update  $R$ .

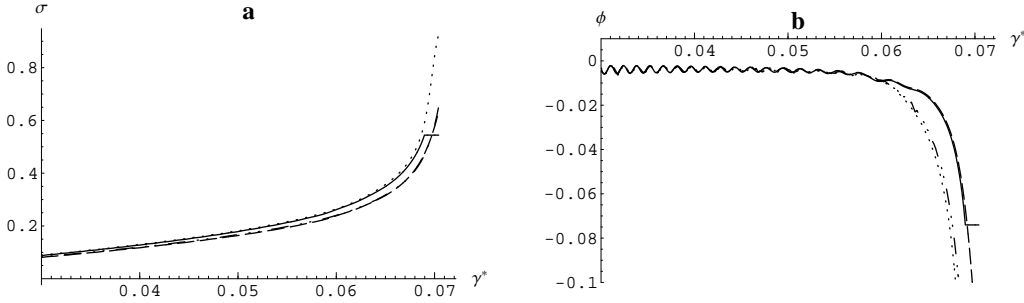


FIGURE 9. (a) Evolution of the eccentricity as a function of the strain for  $\tau = 2500$ . For CS:  $-\cdot-$ ,  $\sigma(0)$ ;  $\cdots$ ,  $\sigma(0.6)$ . For EM+C:  $---$ ,  $\sigma(0)$ ;  $---$ ,  $\sigma(0.6)$ . (b) Evolution of the orientation  $\phi$  for the same case. The EM+C curves for the radius  $r = 0.6$  level off after the elimination of this contour.

Notice that the vorticity contained within the exterior disk does not disappear instantly from the model; part of it is stored temporarily in the corners to be consistent with the observations in § 2. This vorticity is important for the quantitative accuracy of the model.

## 5. Erosion and its relation to equilibria in fixed strain

### 5.1. Comparison

We next compare the solutions of the EM+C for a parabolic vortex in growing strain with direct numerical simulations performed using the CS algorithm. Figure 9 compares the evolution of the eccentricity and of the vortex orientation, calculated in CS using (2.3) and (2.4), for growing adverse shear with  $\tau = 2500$ . The eccentricity differs little between the EM+C and CS during the entire time period. The orientation predicted by the EM is practically identical to that of CS until the onset of erosion. Then, it evolves slower in the EM+C. Figure 9(a) also shows that the eccentricity never varies by more than 10% within the vortex and thus supports the uniform- $\sigma$  approximation made in § 4.4. Figure 10(a) shows the evolution of the squared vortex radius, computed from the area of the separatrix divided by  $\pi$ , for several values of  $\tau$ , and for both the EM+C and CS. The excellent comparison shown here demonstrates that, in spite of the orientation discrepancy, the EM+C is also able to model the erosion and breaking of the vortex. It is striking that even during the last phase of breaking, when the quasi-stationary hypothesis of the EM+C is no longer valid, the discrepancy with respect to CS is limited to the orientation. Similar results have been found for the pure strain case shown in figure 10(b).

In both cases, the breaking strain  $\gamma_b$  depends on the strain growth rate. Figure 11(a) shows that  $\gamma_b$  decreases as the strain growth decreases tending, seemingly, to an asymptotic value close to 0.0675 in the adverse shear case. (In this section, all strain values are assumed to be normalized on the peak vorticity  $\omega_0$ .) This value is significantly smaller than the breaking value for a uniform elliptical patch, which is  $\gamma_m = 3/2 - \sqrt{2} = 0.0857864\dots$  for adverse shear. The reasons for this difference are discussed next.

### 5.2. Stationary equilibrium states

Our numerical results indicate that, for slowly growing strain, a vortex evolves adiabatically, remaining close to equilibrium for much of its lifetime. This suggests that there are nearby equilibrium states, for fixed values of the strain, which attract the vortex evolution, at least until the final breaking. This breaking may be due to a loss of stability of the nearby equilibrium or simply the non-existence of equilibria for strain values exceeding the breaking strain.

To verify that the observed evolution, before breaking, remains close to equilibrium, we have computed the exact equilibria for a family of truncated distributed vortices whose vorticity is zero for  $r > R$  ( $R < 1$ ). In CS, these states have been obtained using the iterative scheme developed

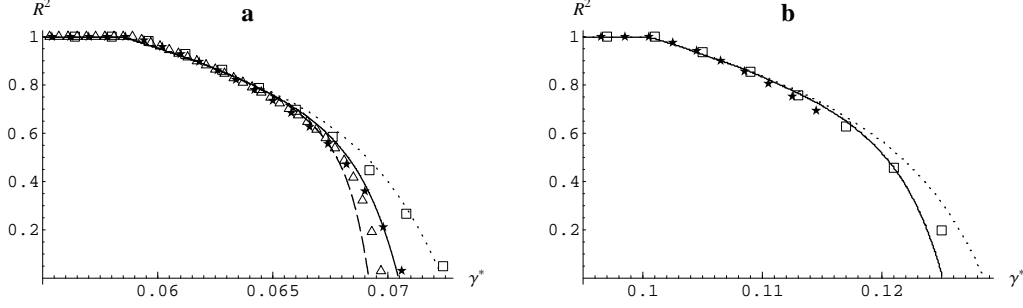


FIGURE 10. (a) Erosion of the vortex as shown by the mean-squared radius of the separatrix after the onset of erosion as a function of the normalised strain  $\gamma^*$  (note:  $R^2 = 1$  before the onset of erosion). For CS:  $\square$ ,  $\tau = 1250$ ;  $\star$ ,  $\tau = 2500$ ;  $\triangle$ ,  $\tau = 5000$ . For EM+C:  $\cdots$ ,  $\tau = 1250$ ;  $---$ ,  $\tau = 2500$ ;  $---$ ,  $\tau = 5000$ . (b) The same for the pure strain case. For CS:  $\square$ ,  $\tau = 500$ ;  $\star$ ,  $\tau = 1000$ . For EM+C:  $\cdots$ ,  $\tau = 500$ ;  $---$ ,  $\tau = 1000$ .

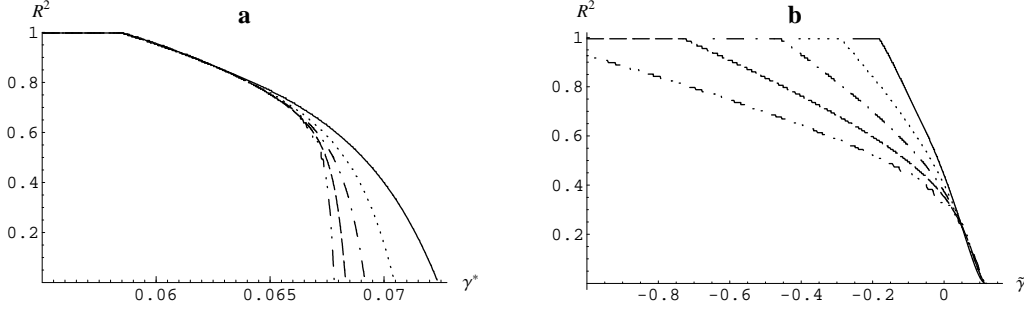


FIGURE 11. (a) Erosion curves for the EM+C defined as in figure 10.  $---$ ,  $\tau = 1250$ ;  $\cdots$ ,  $\tau = 2500$ ;  $-\cdot-\cdot-$ ,  $\tau = 5000$ ;  $---$ ,  $\tau = 10000$ ;  $-\cdot\cdot\cdot$ ,  $\tau = 20000$ . (b) The same after rescaling  $\gamma^*$  into  $\tilde{\gamma} = (\gamma^* - \gamma_c)(\tau\omega_0)^{2/3}$ .

in Dritschel (1995) (see the appendix therein). The area within each vorticity contour (of the 20 used) is fixed, along with one of the following three parameters: the vortex radius  $R$ , the strain rate  $\gamma^*$ , or the positive  $y$ -intercept of the outermost contour with the  $y$ -axis (i.e. the major-axis length of the vortex). One of these three parameters is then varied slowly, and the condition of steady motion determines the third. Depending on the choice of fixed and varying parameters, one can arrive at distinct families of equilibria, at least over small but finite parameter ranges. There can be, for example, several solutions for the same strain rate (see below). Similarly, we have computed the equilibria for the EM with and without the corner contribution (see Appendix C).

In both the EM and CS, we have obtained a limit curve for stationary solutions. In CS, this is reached by varying  $\gamma^*$  or  $R$  until solutions can no longer be found. In the EM, it is obtained directly by introducing the condition for bifurcation degeneracy in the numerical solver. (The corner contribution was not introduced in this version of the EM since the limiting solution does not exhibit corners except in the highly degenerate case  $R = 1$ .) Figure 12(a) shows the two limit curves in the  $(\gamma^*, R)$ -plane. They join at  $\gamma^* = \gamma_m$  for  $R = 0$ , implying by continuity that they extend the turning point of the stationary elliptical patch to distributed vortices. The two curves are very close up to  $R^2 = 0.6$ . For larger values of  $R$ , the EM curve progressively departs from the CS curve. At  $R = 1$ , the EM curve exhibits a spurious turning point, an artefact of the model. Notably, as  $R \rightarrow 1$ , the CS limit solution develops corners, something not accounted for in the EM stationary solver used in this figure.

By incorporating the corner contribution and imposing the condition  $\mathcal{A}_S = \pi R^2$ , we can obtain another solution branch, now for the EM+C, which corresponds to finding stationary solutions with  $\phi = 0$  to the time-dependent model described in § 4.5. The algorithm used to obtain these solutions is described in appendix C. This branch could not be found with the contour-dynamics

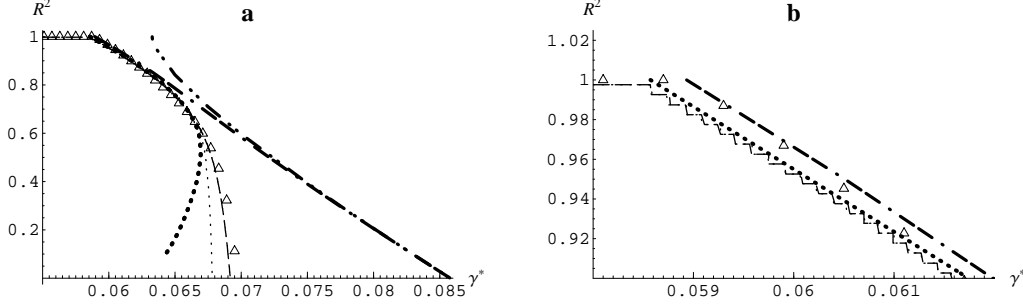


FIGURE 12. Erosion curves and limit branches of stationary solutions. (a)  $\Delta$ , Erosion curve for CS and  $\tau = 5000$ ;  $---$ , erosion curve for the EM+C and  $\tau = 5000$ ;  $\cdots$ , erosion curve for the EM+C and  $\tau = 20000$ ; bold  $---$ , turning line of the mode-2 bifurcation in CS; bold  $-\cdots$ , turning line of the mode-2 bifurcation in the EM; bold  $\cdots$ , branch of stationary solutions with corners in the EM+C. (b) Enlargement of the upper left part of (a) near  $R = 1$ .

iterative scheme, possibly because such corners render the iterative scheme numerically unstable (except at  $R = 1$ ). Figure 12(a) and the enlargement in figure 12(b) shows that this corner branch departs from  $R = 1$  extremely close to the limit CS solution. It exhibits a turning point at  $R_c^2 = 0.51\dots$  and  $\gamma_c = 0.06695\dots$  from which a secondary branch departs towards lower  $R^2$  and  $\gamma^*$ . The time-dependent erosion curves closely track the corner branch from the onset of erosion at  $R = 1$  to the turning point. This turning point coincides with the onset of the fast breaking phase and the dispersion of the erosion curves (here, the evolution becomes sensitive to the strain growth rate).

Therefore, we can explain the observed behaviour of erosion and breaking by the existence of a stable corner solution in a limited range of  $\gamma^*$ . Under slowly growing strain, the distributed vortex first undergoes quasi-stationary erosion with weak oscillations about the family of corner solutions parametrized by  $\gamma^* < \gamma_c$ , and then enters a second, highly unsteady phase of fast breaking when  $\gamma^* \gtrsim \gamma_c$ .

### 5.3. Breaking

It is natural to expect that the turning point of the corner branch is a bifurcation with eigenvalues behaving as  $|\gamma^* - \gamma_c|^{1/n}$ . Since  $\gamma^* - \gamma_c = (t - t_c)/\tau$ , we can infer that the time dependence in the vicinity of the bifurcation is contained in a term of the form

$$\int_{t_c}^t \left( \frac{s - t_c}{\tau} \right)^{1/n} ds = \frac{n}{n+1} \tau (\gamma^* - \gamma_c)^{(n+1)/n}.$$

Accordingly, we have redrawn the curves of figure 11(a) with a new abscissa  $\tilde{\gamma} = (\gamma^* - \gamma_c)(\omega_0 \tau)^{n/n+1}$  for various values of  $n$ . It turns out that the curves best collapse to a single curve for  $n = 2$  as shown in figure 11(b).

One might be tempted to attribute this behaviour to a simple turning point in a one-dimensional space described by the normal form  $\dot{x} = \mu - x^2$  where  $\mu$  is the bifurcation parameter; however, it cannot be that simple since the unstable solution on the secondary branch cannot gain the vorticity required to increase the vortex radius. It was not possible to do the same analysis with the CS curves because we were unable to obtain the location of the turning point on the corner branch. We leave the detailed investigation of the bifurcation structure for further work.

### 5.4. Bifurcations and corners

We have so far demonstrated that the behaviour of a distributed vortex under growing strain differs markedly from that of an elliptical patch. We have, however, found that the turning point which leads to the breaking of the elliptical patch ( $R = 0$ ) extends continuously to distributed

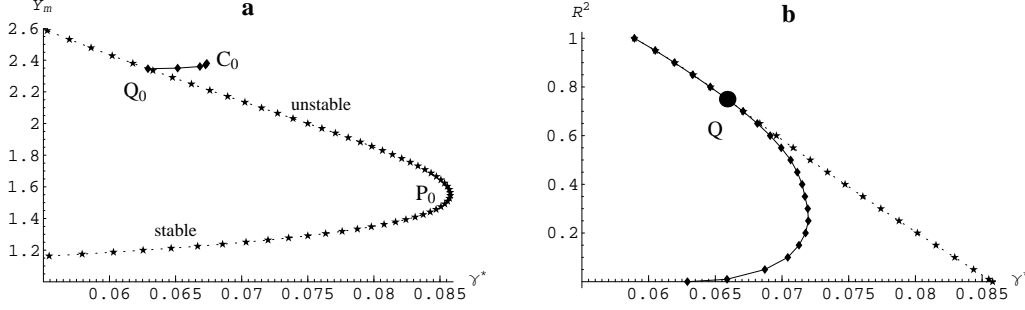


FIGURE 13. (a) Detail of the bifurcation diagram of the stationary vorticity patch within an adverse shear where  $Y_m$  is the semi-major axis length of the vortex. Dotted line and  $\star$ : elliptical solution exhibiting a regular turning point at  $P_0$ . Solid line and  $\blacklozenge$ : branch bifurcating from the “mode-4” instability on the unstable elliptical branch at  $Q_0$  and leading to a corner patch solution at  $C_0$  which is also a regular turning point. Another branch, not shown, extends the solid line across  $Q_0$ , leading to a peanut shaped solution. (b) Stability diagram of the CS equilibrium states within an adverse shear obtained by continuation as indicated in the text. Dotted line and  $\star$ :  $\gamma^* = \gamma_m(R)$ , the regular turning point of the “mode-2” instability. Solid line and  $\blacklozenge$ :  $\gamma^* = \gamma_4(R)$ , the “mode-4” instability. The two curves are tangent at  $Q$  ( $R^2 = 0.75, \gamma^* = 0.6589$ ).

vortices ( $R > 0$ ). This raises the question of why the temporal evolution leads to the limit branch, in one case, and to the corner branch, in the other. It is known (Saffman 1992, p. 174) that the stationary elliptical patch exhibits a “mode-4” transcritical bifurcation at  $\gamma^* = \gamma_4 = 0.062907\dots$  for the pure adverse shear. (Mode  $m$  refers to a disturbance of the form  $\exp(im\eta)$ , where  $\eta$  is the angle variable in elliptical coordinates.) This bifurcation has little dynamical importance because it occurs on the unstable branch bifurcating at  $\gamma^* = \gamma_m$ , i.e. past the turning point (itself a “mode-2” regular bifurcation). Therefore, a patch follows the stable branch from the circular shape all the way to the turning point as found in § 3. It then breaks because there are no steady solutions with greater strain. It is notable that one of the two branches bifurcating at  $\gamma^* = \gamma_4$  leads to a patch solution with a corner (the other one leads to a peanut-shaped vortex). These results are summarized in figure 13(a), showing the semi-major axis length of the vortex versus the strain rate for the patch case.

The existence of a corner limit solution for the vortex patch suggests that the “mode-4” bifurcation may play a role in vortex erosion for distributed vortices. To clarify this, we have carried out a linear stability analysis of the full CS equilibria for fixed truncation  $R$ , following the procedure outlined in Dritschel (1995). This analysis revealed that, for  $R^2 < 0.75$ , the “mode-4” bifurcation occurs on the unstable branch beyond the turning point at  $\gamma^* = \gamma_m(R)$ , just as for the vortex patch. The branch before the turning point is stable. Hence, we would expect that all such vortices evolve under slowly growing strain like the vortex patch, i.e. they do not erode before reaching  $\gamma^* = \gamma_m(R)$ . On the other hand, for  $R^2 > 0.75$ , the “mode-4” bifurcation (at  $\gamma^* = \gamma_4(R)$ ) occurs *before* the turning point at  $\gamma^* = \gamma_m(R)$  on the stable branch — see figure 13(b) — and the two bifurcations stay very close between  $R^2 = 0.75$  and  $R^2 = 1$ . (Though not found to play a role here, a “mode-3” bifurcation is always found between the “mode-4” and the “mode-2” bifurcations, the latter being the turning point itself.) Now, a vortex with  $R^2 > 0.75$  evolving under slowly growing strain cannot reach the turning point (and breaking) at  $\gamma^* = \gamma_m(R)$  because the branch between  $\gamma_4(R)$  and  $\gamma_m(R)$  is unstable. Something else must happen, and our calculations for  $R = 1$  indicate that vortex erosion must take place. Moreover, the vortex evolution appears to trace yet another branch of solutions, a stable branch, with (near) corners. The origin of this branch remains unclear, but we believe it emanates from a highly degenerate bifurcation at  $R = 1$ , where the corner solution and the limit turning point are found for the same value of  $\gamma^*$ . One could further unfold the bifurcation structure via a local normal form analysis, but this is beyond the scope of this article.

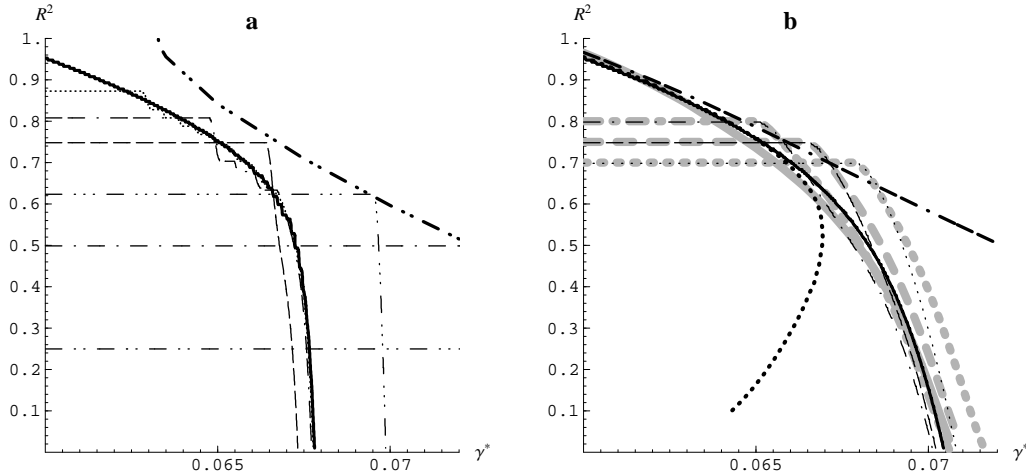


FIGURE 14. Erosion curves for truncated vortices. (a) EM+C for  $\tau = 20000$ . —,  $R_i^2 = 1$ ;  $\cdots$ ,  $R_i^2 = 0.875$ ;  $-\cdot-$ ,  $R_i^2 = 0.81$ ;  $--$ ,  $R_i^2 = 0.75$ ;  $-\cdot\cdot-$ ,  $R_i^2 = 0.625$ .  $\cdots$ , turning line for the mode-2 perturbation in the EM. (b) CS and EM+C for  $\tau = 5000$ . Thick grey lines, CS; thin lines, EM+C;  $-\cdot-$ ,  $R_i^2 = 1$ ;  $-\cdot-$ ,  $R_i^2 = 0.8$ ;  $--$ ,  $R_i^2 = 0.75$ ;  $\cdots$ ,  $R_i^2 = 0.7$ . Bold  $\cdots$ , stationary corner branch in the EM+C; bold  $-\cdot-$ , turning line for the mode-2 bifurcation in CS.

### 5.5. Erosion of truncated vortices

To see how the above bifurcation structure affects the evolution of a vortex under slowly growing strain, we have conducted a number of CS and EM+C simulations of vortices with different initial radii  $R$  under growing adverse shear. The results are summarized in figure 14, showing the mean-squared vortex radius  $R^2$  versus  $\gamma^*$ . The left-hand side shows the results of the EM+C simulations with  $\tau = 20000$ . These results confirm that “patch-like” vortices with  $R^2 < 0.75$  reach the turning point and break before any erosion of edge vorticity takes place ( $R^2$  remains constant up to the turning point and falls precipitously thereafter). On the other hand, the vortices initially with  $R^2 > 0.75$  are clearly attracted to the corner solution branch, the more so the larger the initial  $R$ . These vortices erode, shedding edge vorticity in order to stay near this branch, until breaking finally occurs near the corner-solution turning point at  $R_c^2 = 0.51\dots$  and  $\gamma_c = 0.06695\dots$ . The critical case,  $R^2 = 0.75$ , exhibits a large overshoot, very nearly reaching the turning point at  $\gamma^* = \gamma_m(R)$  before falling briefly back on the corner solution branch and then breaking. The right-hand side shows the results of both the EM+C and CS simulations for  $\tau = 5000$ . Delayed breaking is still observed for  $R^2 < 0.75$  but breaking is slower and significant overshoot is observed with respect to the turning line. Notice again the good agreement between CS and EM+C.

### 5.6. Unsteadiness

One might expect that the above general picture holds more and more accurately as the rate of strain growth tends to zero. The strain growths considered so far are already slow compared to what one might reasonably expect in general (for instance in turbulence), so what happens at still smaller strain growths is perhaps academic. Yet, what happens turns out to be surprising. In a CS simulation conducted using  $\tau = 10000$ , quasi-steady evolution is observed as in all other cases significantly beyond the onset of stripping. Then, at  $\gamma^* = 0.065$ , the vortex momentarily stops stripping (something which does not occur at faster strain growths) and it begins to tumble. The period of unsteadiness lasts for only a few units of time, after which the vortex recovers and begins stripping in a quasi-equilibrium way again. However, periods of unsteadiness occur repeatedly thereafter, followed by temporary recovery, up until the final breaking. This unsteadiness is seen, for example, by the large excursions in the phase discrepancy shown in figure 15(a).

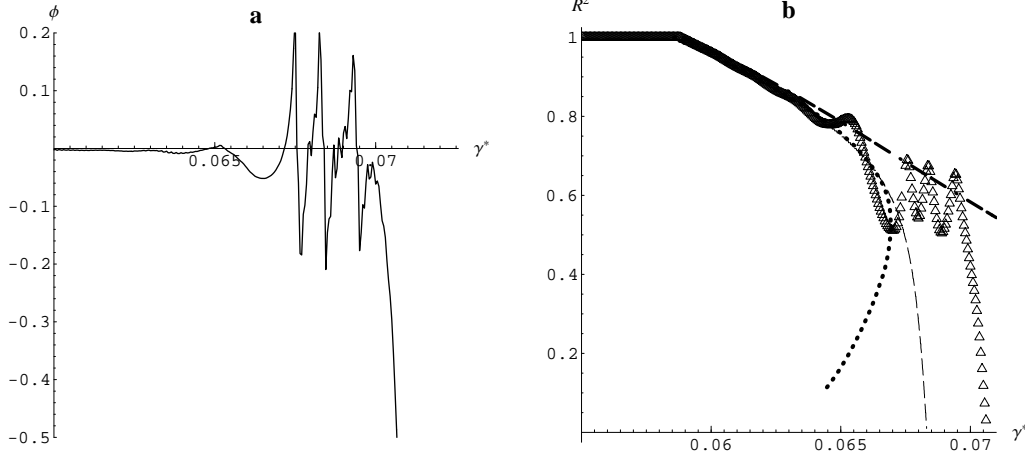


FIGURE 15. Oscillations of the vortex as it passes the mode-4 bifurcation during the erosion in a CS simulation with  $\tau = 10000$ . (a) Oscillations of the orientation  $\phi$  of the vortex core as a function of  $\gamma^*$ . Compare with figure 9. (b)  $\Delta$ , Radius of the vortex (defined as in figure 10). Other curves are as in figure 12(a).

This unsteadiness has a significant effect on the rate of stripping, as seen by the strange behaviour of  $R^2$  versus  $\gamma^*$  in figure 15(b). The large oscillations here occur because the separatrix expands well beyond the vortex edge during the periods of unsteadiness. Moreover, the unsteadiness delays the final breaking relative to the case with twice faster strain growth, which runs contrary to the trend exhibited by the three cases with faster strain growths.

In fact, cases with faster strain growth show traces of this periodic unsteadiness, but it is not enough to stop stripping and cause the vortex to tumble. We have no simple explanation for this behaviour, but believe that it is related to the proximity of unstable solution branches. Indeed, there is numerical evidence that a mode-4 instability occurs for  $\gamma^* = 0.065$  on the corner solution. It is noteworthy that the EM exhibits unsteadiness, with external ellipses crossing, for the same value of  $\gamma^*$  but for much slower strain growths ( $\tau = 40000$ ). Within the EM, modes of order larger than 2 are partially accounted for by the interaction between non-confocal ellipses. We conjecture that the unsteadiness at extremely slow strain growths occurs because the vortex spends too long near the mode-4 bifurcation and wanders enough along its centre manifold to excite tumbling. It is also noteworthy that the reflectional symmetry of the vortex is progressively less well maintained as  $\tau$  increases; this is a hint that the mode-3 instability may be involved in the observed unsteadiness (in addition to mode-4).

## 6. The role of viscosity

In this section, we consider the combined effects of viscosity and growing strain in vortex decay.

The problem of a passive scalar diffusing within a dipolar vortex and across separatrices has already been studied by Lingeitch & Bernoff (1994). The diffusion of vorticity has not been treated as far as we are aware, but there are a number of closely related earlier works (Lamb 1932; Batchelor 1967; Ting & Klein 1991; Saffman 1992; Rhines & Young 1982) which examined nearly steady flows with closed streamlines. Here, we have the added complication that the background straining flow can force a large gradient of vorticity at the vortex edge, and consequently enhanced diffusion there, where streamlines open up to infinity.

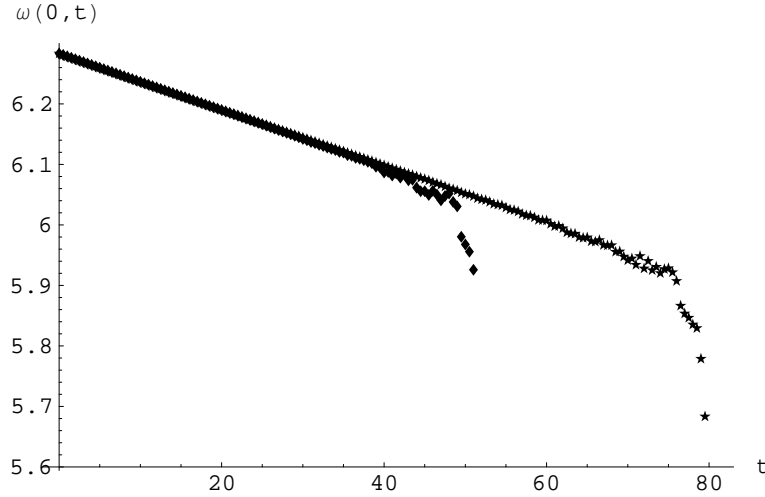


FIGURE 16. Evolution of the maximum vorticity at the centre of the vortex.  $\blacklozenge$ , experiment 1;  $\star$ , same as experiment 1 but with half the strain growth rate. Solid line, curve predicted by (6.3).

### 6.1. Interior decay

In the interior of the vortex, we have seen (e.g. in the weakly-viscous simulation presented in figure 1) that vorticity contours closely match streamlines when the vortex evolves slowly. A passive scalar would also tend to homogenize along a streamline by diffusion over a time scale  $t_h \sim \nu^{-1/3} (\partial(1/T)/\partial r)^{-2/3}$ , where  $T = \oint_{\psi} 1/|\nabla\psi| ds$  is the period of motion along a closed streamline. Small-scale vorticity fluctuations are liable to the same effect though they can also be dissipated by instability and cascade (Dritschel 1989). Consequently, diffusion mainly acts across streamlines for quasi-stationary motion and over time-scales larger than  $t_h$ . It is then possible to derive the equation (Rhines & Young 1983; Lingeitch & Bernoff 1994)

$$\frac{\partial\omega}{\partial t} = \frac{\mathbf{v}}{T(\psi)} \frac{\partial}{\partial\psi} \left( \Gamma(\psi) \frac{\partial\omega}{\partial\psi} \right), \quad (6.1)$$

where  $\psi$  is used as the “radial” coordinate and  $\Gamma(\psi)$  is the circulation within the streamline. It can be shown that a similar equation can be derived within the simplified framework of the elliptical model:

$$\frac{\partial\omega}{\partial t} = \frac{\mathbf{v}}{r} \frac{\partial}{\partial r} \left( r \frac{1 + \sigma^2}{1 - \sigma^2} \frac{\partial\omega}{\partial r} \right). \quad (6.2)$$

Since  $\sigma$  varies much less than  $\omega$  with  $r$ , (6.2) means that the viscous decay inside the vortex is essentially identical to that of an axisymmetric vortex but with a viscosity multiplied by the factor  $(1 + \sigma^2)/(1 - \sigma^2)$ , which remains close to unity until the beginning of the erosion. For an initially parabolic profile,  $\omega(r, t = 0) = \omega_0(1 - r^2/r_0^2)$ , the temporal evolution of the axisymmetric profile is

$$\omega(r, t) = \omega_0 \left( 1 - \frac{4\nu t}{r_0^2} - \frac{r^2}{r_0^2} \right), \quad (6.3)$$

in other words, just a linear decay of the maximum vorticity. Figure 16 shows the decay of the maximum vorticity in experiment 1 and in another experiment with all the parameters identical but with half the strain growth rate. The two curves decay at the same rate, very close to the prediction of (6.3).

### 6.2. The boundary layer

On the separatrix, the period  $T$  goes to infinity and a boundary layer of width  $v^{1/2}$  is formed in its vicinity between the two critical points. A prototype problem where curvature effects are eliminated is provided by the stationary advection-diffusion equation

$$u \frac{\partial \omega}{\partial s} - n \frac{du}{ds} \frac{\partial \omega}{\partial n} = v \frac{\partial^2 \omega}{\partial n^2}, \quad (6.4)$$

which is written for a non-divergent flow with  $(u, v) = (u(s), -n \partial u / \partial s)$  between the two critical points located at  $(0, 0)$  and  $(a, 0)$ . Here  $s$  and  $n$  are respectively the coordinate along and normal to the separatrix. The tangential velocity  $u$  is assumed to vanish at  $s = 0$  and  $a$  and to take a maximum value in the middle of the interval. This equation is a reasonable approximation except in the vicinity of the critical point. Although we introduce it here heuristically, it can be derived from the equations of motion by a change of variable (Lingevitch & Bernoff 1994). Introducing  $\omega = f(\eta)$  with  $\eta = n/\delta(s)$ , we obtain

$$u \delta \frac{d\delta}{ds} + \frac{du}{ds} \delta^2 = -v \frac{f''}{\eta f'}, \quad (6.5)$$

where  $\mu$  is the separation constant. The solution to the transversal problem (in  $\eta$ ) is the error function

$$f = f_0 \int_{-\infty}^{\eta} \exp(\mu p^2 / 2v) dp, \quad (6.6)$$

assuming that the vorticity vanishes for  $n \rightarrow -\infty$  and takes a uniform value  $\omega_e$  as  $n \rightarrow \infty$ . Then we have  $\omega_e = f_0 (2\pi v / \mu)^{1/2}$ . Therefore, a convenient choice is  $\mu = 2\pi v$  for which  $\omega_e = f_0$ . The longitudinal equation then reduces to

$$\frac{d}{ds} (\delta u)^2 = 4\pi v u. \quad (6.7)$$

Assuming now that  $u(s) = u_0 \sin \pi s / a$  we obtain

$$\delta^2 = \frac{4va}{u_0} \left( \frac{1}{1 + \cos(\pi s/a)} + \frac{K}{\sin^2(\pi s/a)} \right), \quad (6.8)$$

where we take  $K = 0$  in what follows to eliminate the singularity at the converging hyperbolic point  $s = 0$ .

We can use this solution to estimate the diffusive flux  $F_v$  across the separatrix as

$$F_v = \int_0^a v \frac{\partial \omega}{\partial \eta} ds = v f_0 \int_0^a \frac{1}{\delta} ds.$$

Using (6.8), we get

$$F_v = \frac{1}{\sqrt{2\pi}} \omega_e (v a u_0)^{1/2}. \quad (6.9)$$

Notice that taking  $K \neq 0$  does not change the scaling of  $F_v$ . If this flux is to match the internal diffusion described by (6.2), which is  $O(v)$ , the condition  $\omega_e = O(v^{1/2})$  is required. Therefore, a pure viscous decay cannot preserve a high gradient on the separatrix. This result corroborates that of Lingevitch & Bernoff (1994) obtained under more general conditions.

### 6.3. Separation of the boundary layer

We have so far assumed that the velocity is purely stationary and that the vorticity is a passive scalar. In fact, the separatrix is not stationary but retreats inward because of the decrease of the vortex circulation and the increase of the strain. Assuming a uniform retreat velocity  $v_0$  which is

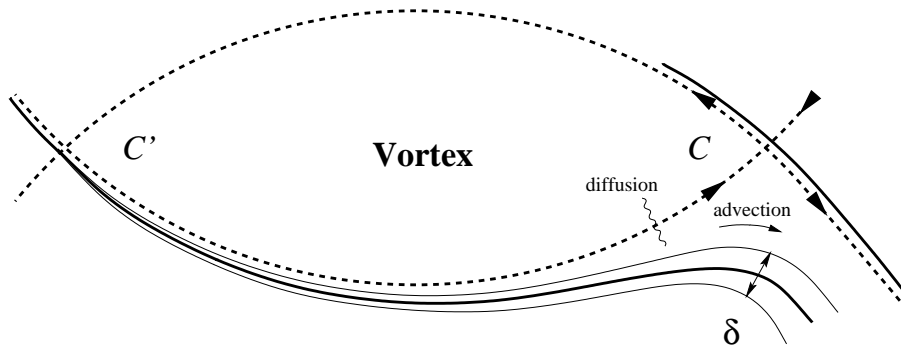


FIGURE 17. Separation of the boundary layer from an eroding vortex.

related to the strain growth in Appendix D (cf. (D 6)), one may generalize the stationary equation (6.4) to a frame of reference moving with the separatrix:

$$u \frac{\partial \omega}{\partial s} - n \frac{du}{ds} \frac{\partial \omega}{\partial n} - v_0 \frac{\partial \omega}{\partial n} = \nu \frac{\partial^2 \omega}{\partial n^2}. \quad (6.10)$$

This equation has the same solution as (6.4) satisfying (6.5) but for  $\eta$  which is now defined as  $\eta = (n - n_0)/\delta$  and where  $n_0(s)$  is governed by

$$\frac{\partial n_0 u}{\partial s} = -v_0.$$

Therefore, the edge is centred on the curve

$$n_0(s) = -\frac{sv_0}{u(s)}$$

which diverges from the separatrix as  $s$  runs from 0 to  $a$ . The condition of separation of the boundary layer is that  $n_0(s) > \frac{1}{2}\delta(s)$  when  $s$  approaches  $a$ . When this is satisfied, as sketched in figure 17, the boundary layer separates from the separatrix and the interior viscous flux is essentially matched by retreat and advection. This allows a steep gradient to form at the vortex edge, consistent with figure 1.

For  $u = u_0 \sin(\pi s/a)$ , the separation condition reads

$$v_0 > (2\nu u_0/a)^{1/2}, \quad (6.11)$$

which is satisfied by experiment 1 as shown in Appendix D and in agreement with figure 6(a).

## 7. Discussion

We have presented a simplified model for the erosion and breaking of a distributed two-dimensional vortex subjected to slowly growing strain. The model approximates the vortex by a nested stack of elliptical vorticity contours, all having the same orientation, and includes procedures for removing external contours during the inward penetration of the critical points and for approximating the immediate effects of these eroded contours. Comparisons with full, two-dimensional flow simulations show that the proposed model is quantitatively accurate. This accuracy depends crucially on taking into account the effects of the eroded contours, here in the form of corner regions in the vicinity of the critical points. Although the simplified model was intended to provide physical insight and not as a numerical tool, it is noteworthy to mention that simulations require only a couple of minutes on a standard PC while the corresponding CS simulations require tens of hours on a Cray XMP.

More fundamentally, we have shown that stripping or erosion can be most easily understood in

the context of a slowly changing external flow field. This is a natural context when vortices are not strongly interacting, as in vortex merger (Dritschel 1995). Then, the vortex evolves adiabatically, or nearly so, tracking close to equilibrium states. It is remarkable that this remains the case when the vortex begins to erode; even the loss of material from the vortex edge is slow enough to allow the nearly adiabatic evolution to continue. At sufficiently large strain, there are no further nearby (stable) equilibria, and breaking occurs.

While often the external flow changes slowly, it is rare for it to change as slowly as the exceptional case pointed out in § 5.6, and so the peculiarities of this case are not likely to be seen in practice. What we have learned from this case is that the stability properties of the nearby equilibrium state or states generally influences the behaviour of the vortex. Spending too long near the cross-roads of two states leads to transient, time-dependent behaviour. Under typical rates of strain growth or decay, a vortex passes such places too quickly and at sufficient distance to be significantly disturbed.

We have considered the effect of viscosity on stripping. Its effect depends on the rate of strain growth. If this rate is sufficiently small, then the vortex diffuses in the normal way, i.e. like a Lamb–Oseen vortex (Lamb 1932), with its interior circulation (that contained within the curve of highest vorticity gradient) decaying at a rate proportional to  $\nu$ , where  $\nu$  is the viscosity. There is a viscous boundary layer of  $O(\nu^{1/2})$  width sitting over or very close to the separatrix but no associated sharp vorticity gradient. On the other hand, for larger strain growth, the decay of circulation is slightly enhanced by the ellipticity but the most striking effect is the generation and maintenance of a sharp vorticity jump across the viscous boundary layer which detaches from the separatrix, with the vorticity between the boundary layer and the separatrix being deposited into a filament expelled into the surrounding flow. Now, if the strain ceases to be applied before reaching vortex breaking it is clear that the diffusion of the steep gradient towards the inside of the vortex will accelerate circulation decay. If the strain is applied repetitively up to the same subcritical value, the viscous decay will be greatly enhanced through a repeated cycle of steep gradient regeneration and diffusion.

The presence of a steep gradient is often associated with the presence of a barrier to transport (Chen 1994; Waugh *et al.* 1994; Waugh 1996). We demonstrate here that in the presence of diffusion the maintenance of steep gradients comes along with a finite rate of stripping, and therefore an exchange between the vortex and the exterior.

A practically important extension of this work would be to consider three-dimensional vortices in a rotating, stratified fluid (of which the atmosphere and oceans are good examples). Stripping is likely to generate or maintain sharp gradients of potential vorticity at the periphery of vortices (as in the case of the polar stratospheric vortex (Tuck 1989)), and along fronts and jets (as in the case of the Gulf Stream (Lai & Richardson 1977)). Apart from the three-dimensionality of the vortical flow, the new effect that must be taken into account is that of vertical shear, which to leading order may be approximated by a linear vertical gradient of the horizontal velocity. Just as in the two-dimensional case considered in this paper, there are exact solutions for uniform vortices, now ellipsoids, in general linear straining flows, including vertical shear (Meacham *et al.* 1994). There is thus a natural starting point to extend the present work to three dimensions.

## Appendix A. The corner

### A.1. Geometry of the corner

The angle  $\theta$  and the length  $\chi$  of its two sides are given by

$$\tan \theta = \frac{\lambda_R R}{(\lambda_R X_C^2 - R^2)^{1/2}}, \quad (\text{A } 1)$$

$$\chi = \frac{\lambda_R X_C^2 - R^2}{\lambda_R X_C \cos \theta}, \quad (\text{A } 2)$$

where  $\lambda_R = (1 - \sigma(R))/(1 + \sigma(R))$  is the aspect ratio of the exterior ellipse.

The area  $A$  of the corner is

$$A(\theta, \chi) = \chi^2 \tan \theta \left\{ 1 - \frac{1}{2}(\pi - 2\theta) \tan \theta \right\}, \quad (\text{A } 3)$$

and the abscissa of its centroid is  $X_C + \hat{X}$  with

$$\hat{X}(\theta, \chi) = -\frac{\chi^3}{6A(\theta, \chi)} \sec \theta \tan \theta (5 - 2 \cos 2\theta + 3(2\theta - \pi) \tan \theta). \quad (\text{A } 4)$$

### A.2. Velocity induced by the corner

The velocity induced at  $z = x + iy$  by a patch of uniform vorticity  $\omega$  is

$$\dot{z} = 2i \frac{\partial \Psi}{\partial \bar{z}} = i \frac{\omega}{2\pi} \iint \frac{1}{\bar{z} - z'} dx' dy' = \frac{\omega}{2\pi} \oint \frac{z' - z}{z' - \bar{z}} d\bar{z}', \quad (\text{A } 5)$$

where we have used Green's theorem to reduce the expression to a contour integral.

Evaluating (A 5) around the contour bounding the corner region defined in the previous subsection, we obtain its contribution to the velocity at its vertex as

$$V_c = \frac{\omega(R)\chi}{4\pi} (2 \sin \theta + \pi \cos \theta - (\pi - 2\theta) \sec \theta). \quad (\text{A } 6)$$

The contribution of the corner to the velocity at a distant point can be approximated by representing the corner as a point vortex located at its centroid and having the same circulation. In particular, the contribution to the velocity at the vertex of the opposite corner is

$$V_{\text{opp}} = \frac{\omega(R)A(\theta, \chi)}{2\pi(2X_C + \hat{X}(\theta, \chi))} \quad (\text{A } 7)$$

### A.3. Contribution of the corners to the elliptical model

The two corners are approximated by point vortices as above. Assuming alignment with the axis of the ellipse  $\{r, \sigma\}$  they induce a rotation (Legras & Dritschel 1991) which contributes to the right-hand side of (4.1) as

$$\frac{\partial}{\partial t} m(r) \leftarrow i \frac{\omega(R)(1 - \sigma^4(r))}{\pi r^2 \sigma^2(r)} mA(\theta, \chi) \tan^2 \frac{v_r}{2}, \quad (\text{A } 8)$$

where  $v_r$  is given by (4.3) with  $X = X_C + \hat{X}(\theta, \chi)$ .

### A.4. Contribution of the corner to the streamfunction

We need the streamfunction at the critical point and at other points on the separatrix which are distant from the critical point. For distant points, we approximate each corner by a point vortex located at its centroid. Hence, the contribution of the corners to the streamfunction at a point

located outside the vortex and distant from the corners is

$$\begin{aligned} \psi_C(X, Y) = \frac{\omega(R)}{4\pi} A(\theta, \chi) \{ & \ln[(X - X_C - \hat{X}(\theta, \chi))^2 + Y^2] \\ & + \ln[(X + X_C + \hat{X}(\theta, \chi))^2 + Y^2] \}. \end{aligned} \quad (\text{A } 9)$$

where  $(X, Y)$  are coordinates with respect to the rotating axis of the vortex.

The contribution of the neighboring corner to the streamfunction at the critical point (the vertex of the corner) can be calculated as a contour integral using the following relation for a uniform vorticity patch:

$$\psi(z) = \frac{\omega}{2\pi} \iint \ln|z - z'| dx' dy' = \frac{\omega}{4\pi} \Im \left\{ \oint \bar{z}' \ln(z' - z) dz' \right\}. \quad (\text{A } 10)$$

Evaluating (A 10) at the corner, we obtain after some algebra

$$\begin{aligned} \psi_C(X_C, 0) = \frac{\chi^2 \omega(R)}{4\pi} \left\{ \theta + \tan \theta ((2\theta - \pi) \tan \theta + 2) \ln \chi - 2 \right. \\ \left. + 2\theta \tan \theta \ln \sin \theta + 2 \sum_{k=1}^{\infty} \cos^{k-1} \theta \frac{\sin k\theta}{k^2} \right\} \\ + \frac{\omega(R) A(\theta, \chi)}{2\pi} \ln[2X_C + \hat{X}(\theta, \chi)]. \end{aligned} \quad (\text{A } 11)$$

## Appendix B. Calculation of the separatrix

The separatrix is approximated as the polynomial function

$$Y = p + qX^2 + rX^4 + sX^6$$

in the coordinates  $(X, Y)$  relative to the axes of the vortex. Because of the non-symmetric  $XY$  term in (4.6) the separatrix is symmetric with respect to the centre of the vortex but not with respect to its axes. We therefore need to calculate two sets of coefficients  $(p_a, q_a, r_a, s_a)$  and  $(p_b, q_b, r_b, s_b)$  that will be used respectively in the first and the third quadrants of the  $(X, Y)$ -plane, and in the second and the fourth quadrants.

The coefficients are determined by finding a few points on the separatrix. The first one is the critical point and the other ones are obtained by solving  $\psi(X, Y) = \psi(X_C, 0)$  along fixed directions by a secant method. In particular we find the intersection  $Y_S$  of the separatrix with the minor axis. Two other points are obtained in the first and second quadrant along the directions  $(\varphi_1, -\varphi_1, \varphi_2, -\varphi_2)$ . The coefficients are then calculated to ensure that the polynomial passes through the four points. We have taken  $\varphi_1 = \pi/10$  and  $\varphi_2 = \pi/5$ , but the results are not sensitive to these values.

The area of the separatrix is then estimated as

$$\mathcal{A}_S = 2(p_a + p_b)X_C + \frac{2}{3}(q_a + q_b)X_C^3 + \frac{2}{5}(r_a + r_b)X_C^5 + \frac{2}{7}(s_a + s_b)X_C^7. \quad (\text{B } 1)$$

### Appendix C. Stationary solutions of the elliptical model

The equilibrium states for the EM+C where the vortex is aligned with the direction  $\phi = 0$  are obtained from (4.1) and (A 8), that is

$$\begin{aligned} & 2\lambda(r)\sigma(r)H - \frac{(1-\sigma(r))^2}{r^4} \int_0^r \frac{\sigma(s)}{1-\sigma^2(s)} s^4 \omega'(s) ds \\ & + \frac{1+\lambda^2(r)}{2} ((1+\sigma(R))\omega(R) - \int_r^R (1+\sigma(s))\omega'(s) ds) \\ & + (1+\lambda^2(r))\gamma - (1-\lambda^2(r))\Omega - \omega(r) + G = 0 \end{aligned} \quad (\text{C } 1)$$

where

$$G = \frac{2\omega(R)A(\theta, \chi)\lambda(r)(1+\sigma^2(r))}{\pi r^2 \sigma(r)} \tan^2 \frac{\nu_r}{2},$$

with  $\lambda(r) = (1-\sigma(r))/(1+\sigma(r))$  and  $H = 1/r^2 \int_0^r s^2 \omega'(s) dx$ . After differentiation (and some algebra), the integral equation (C 1) is replaced by a second-order differential system

$$\frac{\partial F}{\partial r} = (1+\sigma)\omega', \quad (\text{C } 2)$$

$$F = - \left( \frac{P_1 r \frac{\partial \sigma}{\partial r} + P_2}{Q_1 r \frac{\partial \sigma}{\partial r} + Q_2} \right), \quad (\text{C } 3)$$

with

$$\begin{aligned} P_1 &= \gamma - \Omega - \lambda^3(\gamma + \Omega) - \omega + G \\ &+ \frac{\lambda(1+\sigma^2)}{(1+\sigma)} H + \frac{1}{2}(1-\sigma) \frac{\partial G}{\partial \sigma}, \end{aligned} \quad (\text{C } 4)$$

$$\begin{aligned} P_2 &= 2(1-\sigma)(\gamma - \Omega + G - \omega + \lambda^2(\gamma + \Omega)) \\ &+ 2\sigma(1+\sigma)\lambda^2 H + \frac{r}{2}(1-\sigma) \frac{\partial G}{\partial r}, \end{aligned} \quad (\text{C } 5)$$

$$Q_1 = \frac{\sigma(1+\lambda+\lambda^2)}{1-\sigma}, \quad (\text{C } 6)$$

$$Q_2 = (1+\lambda^2)(1-\sigma). \quad (\text{C } 7)$$

The boundary conditions for  $F$  at  $r = 0$  and  $r = R$  are

$$F(0) = -2 \frac{\gamma - \Omega + G_0 - \omega(0) + \lambda^2(0)(\gamma + \Omega)}{\sigma(0)(1+\lambda(0)+\lambda^2(0))}, \quad (\text{C } 8)$$

$$F(R) = (1+\sigma(R))\omega(R), \quad (\text{C } 9)$$

with

$$G_0 = \frac{2\omega(R)A(\chi, \theta)(1+\sigma^2(0))}{\pi(X_C + \hat{X})^2(1+\sigma(0))^2}.$$

The stationary limit solution of the EM+C is found in two steps. First, for given values of the strain parameters  $\{\gamma, \Omega\}$  and  $R$ , we make a guess  $\{\sigma_0^*, \sigma_R^*, X_C^*\}$  for the eccentricity at the centre and the edge of the vortex, and for the location of the critical point along the major axis. Then the parameters of the corners are obtained by (A 2–A 4). By integrating (C 2) and (C 3) from  $r = 0$  to  $r = R$  using  $\sigma(0) = \sigma_0^*$  and (C 8) as initial conditions, we obtain  $\sigma(R)$ . Next, the velocity at  $X_C^*$  is obtained from (4.4). We then solve iteratively the set of equations  $\{(C 9), \sigma_R^* = \sigma(R)\}$ ,

$V(X_C^*) = 0\}$ , using a damped Newton's method, for  $\{\sigma_0^*, \sigma_R^*, X_C^*\}$ . Once this solution is obtained, the second step consists of calculating the separatrix and its area according to the algorithm described in section 4.3 and of solving  $\mathcal{A}_S = \pi R^2$  for  $R$  by Brent's method.

This procedure results in a stationary solution with parametrized corners which is marginal for erosion in the sense given in § 4.3. By varying the value of the strain, the curve of marginal stationary solutions is obtained.

The whole method has been implemented as a *Mathematica* notebook which is available on request.

#### Appendix D. Separation of the boundary layer for the Gaussian vortex

In order to test the condition (6.11) we need to estimate  $v_0$  and  $u_0$  for the Gaussian vortex used in experiment 1. In order to simplify the calculation, we assume a uniform eccentricity  $\sigma$  and we neglect the role of the corners in the erosion. That is, we pretend that the separatrix is approximated by an external ellipse. This assumption generates significant error in the prediction of breaking but it can be used here for diagnostic purposes.

Inside the vortex, the Gaussian profile decays as

$$\omega(r, t) = \omega_M(t) \exp\left(-\frac{r^2}{r_M^2(t)}\right),$$

with  $r_M^2 = r_0^2 + 4vt$  and  $\omega_M = \omega_0 r_0 / r_M$ . The complex velocity  $U = u + iv$  at the point  $z = x + iy$  is given by Legras & Dritschel (1991):

$$\overline{U(z)} = 2i\gamma x - i \frac{\omega_M R (1 - \sigma^2)^{1/2}}{2\zeta(z, R)} \exp\left(-\frac{R^2}{r_M^2}\right) - i\omega_M \int_0^r \frac{s^2}{r_M^2 \zeta(z, r)} \exp\left(-\frac{s^2}{r_M^2}\right) ds, \quad (\text{D } 1)$$

where  $\zeta(z, r)$  is the solution of

$$z(1 - \sigma^2)^{1/2} = r \left( \zeta(z, r) + \frac{\sigma}{\zeta(z, r)} \right) = R \left( \zeta(z, R) + \frac{\sigma}{\zeta(z, R)} \right). \quad (\text{D } 2)$$

Under the stated approximations the velocity  $u_0$  is given by

$$u_0 = |U(0, R\lambda^{1/2})|, \quad (\text{D } 3)$$

while the erosion condition is

$$0 = U(R\lambda^{-1/2}, 0), \quad (\text{D } 4)$$

and the retreat rate  $v_0$  is obtained by differentiating (D 4) with respect to  $t$ .

Unlike the case of the parabolic profile, (D 1) cannot be integrated exactly but it can be integrated perturbatively by expanding  $\zeta(z, r)$  as a power series in  $\sigma$ . At leading order, we have  $\zeta(z, r) = R/r\zeta(z, R)$  leading to

$$u_0 = \frac{\omega_M r_M^2}{2R^2} (1 - \sigma^2)^{1/2} \left( 1 - \exp\left(-\frac{R^2}{r_M^2}\right) \right), \quad (\text{D } 5)$$

and

$$\frac{4\gamma}{1 - \sigma} = \omega_0 \frac{r_0 r_M}{R^2} \left( 1 - \exp\left(-\frac{R^2}{r_M^2}\right) \right).$$

Therefore, the retreat velocity is

$$v_0 = -\frac{dR}{dt} = \left( \frac{2\dot{\gamma}R^3}{\omega_M(1 - \sigma)} + \frac{4vR^3}{r_M^2} \exp\left(-\frac{R^2}{r_M^2}\right) \right) \left( r_M^2 - (R^2 + r_M^2) \exp\left(-\frac{R^2}{r_M^2}\right) \right)^{-1} \quad (\text{D } 6)$$

with  $\dot{\gamma} = d\gamma/dt$ . In addition, we have

$$a = 2R \left( \frac{1-\sigma}{1+\sigma} \right)^{1/2} E \left( -\frac{4\sigma}{(1-\sigma)^2} \right), \quad (\text{D } 7)$$

where  $E$  is the complete elliptical integral of the second kind. Using now the values  $r_0 = 0.5$ ,  $R = 0.6$ ,  $\omega_0 = 2\pi$ ,  $t = 42$ ,  $\sigma = 0.4$ ,  $\dot{\gamma}/\omega_0 = 0.0014$  and  $\nu = 5.6 \cdot 10^{-5}$  which are relevant to figure 6(a), we find that the dissipative term in  $\nu$  can be neglected in the r.h.s. of (D 6) and we obtain

$$J \equiv \frac{1}{\nu_0} \left( \frac{2\nu u_0}{a} \right)^{1/2} = 0.69.$$

When the calculation is performed at orders 1 and 2 in  $\sigma$ , we obtain respectively  $J = 0.77$  and  $J = 0.76$ . Therefore the separation criterion is satisfied for the boundary layer.

#### REFERENCES

- BATCHELOR, G. 1967 *An Introduction to Fluid Mechanics*. Cambridge University Press.
- CHEN, P. 1994 The permeability of the Antarctic vortex edge. *J. Geophys. Res.* **99** (D10), 20563–20571.
- DRITSCHEL, D. 1989 Contour dynamics and contour surgery: numerical algorithms for extended, high-resolution modelling of vortex dynamics in two-dimensional, inviscid, incompressible flows. *Computer Phys. Rep.* **10** (3), 77–146.
- DRITSCHEL, D. 1990 The stability of elliptical vortices in an external straining flow. *J. Fluid Mech.* **210**, 223–261.
- DRITSCHEL, D. 1995 A general theory for two-dimensional vortex interaction. *J. Fluid Mech.* **293**, 269–303.
- DRITSCHEL, D. 1998 On the persistence of non-axisymmetric vortices in inviscid two-dimensional flow. *J. Fluid Mech.* **371**, 141–155.
- DRITSCHEL, D. & WAUGH, D. 1992 Quantification of the inelastic interaction of two asymmetric vortices in two-dimensional vortex dynamics. *Phys. Fluids A* **4**, 1737–1744.
- JIMENEZ, J., MOFFATT, H. & VASCO, C. 1996 The structure of the vortices in freely decaying two-dimensional turbulence. *J. Fluid Mech.* **313**, 209–222.
- KIDA, S. 1981 Motion of an elliptical vortex in a uniform shear flow. *J. Phys. Soc. Japan* **50**, 3517–3520.
- LAI, D. & RICHARDSON, P. 1977 Distribution and movement of gulf stream ring. *J. Phys. Oceanogr.* **7**, 670–683.
- LAMB, H. 1932 *Hydrodynamics*. Cambridge University Press.
- LEGRAS, B. & DRITSCHEL, D. 1991 The elliptical model of two-dimensional vortex dynamics. Part I: The basic state. *Phys. Fluids A* **3**, 845–854.
- LEGRAS, B. & DRITSCHEL, D. 1993a A comparison of the contour surgery and pseudo-spectral methods. *J. Comput. Phys.* **104** (2), 287–302.
- LEGRAS, B. & DRITSCHEL, D. 1993b Vortex stripping and the generation of high vorticity gradients in two-dimensional flows. *Appl. Sci. Res.* **51**, 445–455.
- LINGEVITCH, J. F. & BERNOFF, A. J. 1994 An advection of a passive scalar by a vortex couple in the small-diffusion limit. *J. Fluid Mech.* **270**, 219–249.
- LOVE, A. 1893 On the stability of certain vortex motions. *Proc. Lond. Math. Soc.* **35**.
- MARIOTTI, A., LEGRAS, B. & DRITSCHEL, D. 1994 Vortex stripping and the erosion of coherent structures in two-dimensional flows. *Phys. Fluids A* **6**, 3954–3962.
- MEACHAM, S., PANKRATOV, K., SHCHEPETKIN, A. & ZHMUR, V. 1994 The interaction of ellipsoidal vortices with background shear flows in a stratified fluid. *Dyn. Atmos. Oceans* **21**, 167–212.
- MOORE, D. & SAFFMAN, P. 1971 *Structure of a Line Vortex in an Imposed Strain*. Plenum.
- RHINES, P. B. & YOUNG, W. R. 1982 Homeogenization of potential vorticity in planetary gyres. *J. Fluid Mech.* **122**, 347–367.
- RHINES, P. B. & YOUNG, W. R. 1983 How rapidly is a passive scalar mixed within closed streamlines. *J. Fluid Mech.* **133**, 133–145.
- SAFFMAN, P. 1992 *Vortex Dynamics*. Cambridge University Press.
- TING, L. & KLEIN, R. 1991 *Viscous Vortical Flows*, Lecture Notes in Physics, vol. 374. Springer.

- TUCK, A. 1989 Synoptic and chemical evolution of the Antarctic vortex in late winter and early spring. *J. Geophys. Res.* **94**, 11687–11737.
- WAUGH, D. 1996 Seasonal variation of isentropic transport out of the tropical stratosphere. *J. Geophys. Res.* **101**, 4007–4023.
- WAUGH, D., PLUMB, R., ATKINSON, R., SCHOEBERL, M., LAIT, L., NEWMAN, P., LOWENSTEIN, M., TOOHEY, D., AVALLONE, L., WEBSTER, C. & MAY, R. 1994 Transport of material out of the stratospheric Arctic vortex by Rossby wave breaking. *J. Geophys. Res.* **99** (D1), 1071–1088.
- YAO, H. B., DRITSCHEL, D. G. & ZABUSKY, N. J. 1995 High-gradient phenomena in two-dimensional vortex interaction. *Phys. Fluids* **7**, 539–548.